Further studies with DesertACT and performance analysis of a new type of a tiny sized telescope

Master's Thesis in Physics

Presented by
Jelena Mila Ćelić
13.09.2021

Erlangen Centre for Astroparticle Physics
Physikalisches Institut II
Friedrich-Alexander-Universität Erlangen-Nürnberg

Supervisor: Prof. Dr. Stefan Funk

Abstract

To study high-energy cosmic rays and their origin, atmospheric ground-based Imaging Atmospheric Cherenkov Telescopes (IACTs) such as the High Energy Stereoscopic System (H.E.S.S.) or the planned Cherenkov Telescope Array (CTA) are used as the detectors. In this work, the suitability of two such small cost-efficient telescopes (an IceAct telescope and a scaled-down Small Sized Telescope called TinyTel) is evaluated with special emphasis on gamma hadron separation and event reconstruction. Due to background suppression, both are unsuitable as single telescope projects, but still in comparison TinyTel is more precise than the IceAct telescope. One can either improve the background suppression by using a multivariate cut optimization or one extends already existing IACTs with TinyTel. This telescope could be used to extend projects such as H.E.S.S. and CTA in the high energy domain or could be used for public outreach.

Contents

1 Introduction

After the discovery of radioactivity by eminent scientists such as Marie Curie and Henri Berequel, it was known that radioactive materials have an ionising effect due to the emission of charged particles. But at the beginning of the 21st century, Wilson, with the help of many other scientists, made the discovery that ionisation occurs even without the presence of a radioactive material. In 1912, Victor Hess discovered cosmic rays through a series of experiments with a hot air balloon. He measured the ionization levels at different altitudes up to a height of about 5 km. The only explanation for this radiation at that time was the natural radiation of the Earth. Since until now only the radioactivity of the ground was known, it was expected that the radiation would decrease with increasing altitude. However, he found that the radiation increases at higher altitudes. From his new discovery, he concluded that there must be a previously undetected, additional radiation component on Earth that does not emanate from our planet, but rather penetrates the Earth's atmosphere from above, but has remained undetected to this point. In the last hundred years, through many more experiments, it has been discovered that this phenomenon is caused by so called cosmic radiation originating from galactic and extragalatic sources [1, 2].
An important part of modern astrophysics is to study these cosmic rays, consisting of charged and uncharged particles, and their origins. The uncharged component is an excellent candidate because it is not deflected during their propagation through the interstellar medium. To detect gamma rays, many detection methods were invented over the year. One of these methods are ground-based detectors such as the The High Energy Stereoscopic System (H.E.S.S.) in Namibia or the planned Cherenkov Telescope Array (CTA). For the detection of high-energy cosmic rays, a very large detection area is required because of the low flux [3]. Another telescope can be found at the South pole. A candidate for the extension of the IceTop array as part of the Gen2 upgrade is the IceACT telescope used for the event selection [4].
The aim of this work is, on the one hand, to test whether event reconstruction is possible with an existing IceACT telescope which has already been used in the Namibia campaign. On the other hand a new type of tiny telescope is created and simulated and its performance is validated. An overview of cosmic rays, their production mechanisms and their detection is given in the upcoming sections.

2 Cosmic rays

At the beginning of this chapter, a brief introduction to cosmic rays is given with a focus on their spectrum and their production mechanisms. Due to the nature of the work done in this thesis, special emphasis is placed on the processes leading to gamma ray production.

2.1 The Cosmic Ray (CR) spectrum

CR are high-energetic particles, propagating through the interstellar medium. They consist of both charged and uncharged particles. One can distinguish between the so called primary and secondary CR. Primary cosmic rays originate from their source which can be either galatic or extragalactic depending on their energy. Eventually, these particles interact with the nuclei in the earths atmosphere and emit new particles, called secondary CR [5].
The spectrum of CR extends over several magnitudes of energies measured directly with space-based experiments and indirectly with air shower detectors, as shown in figure 1 below.

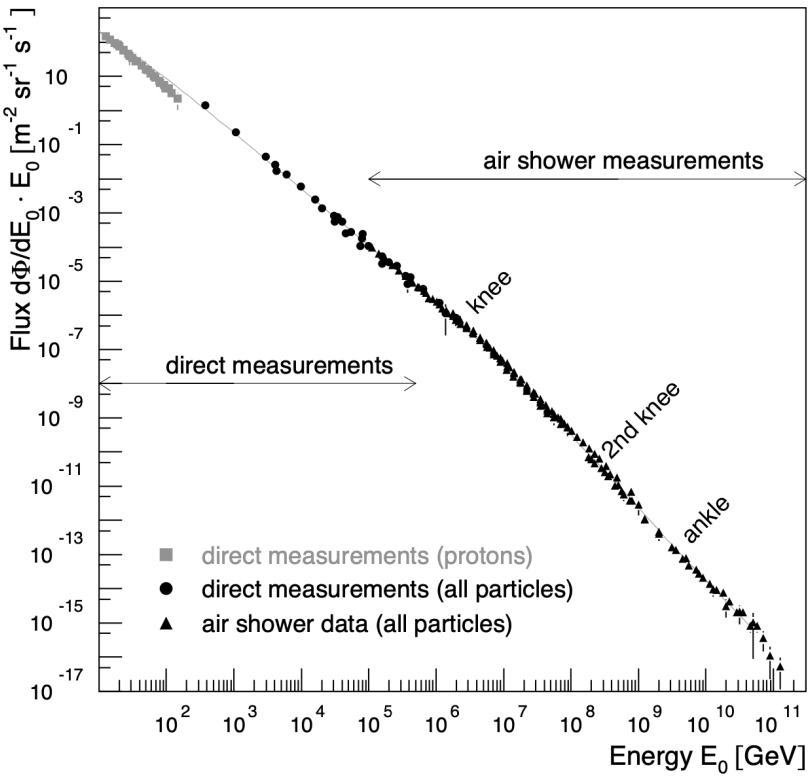

Figure 1: CR energy spectrum measured directly with space-based experiments and indirectly with ground based detectors [6].

It can be approximated by a broken powerlaw with four energy dependent spectral indices $\gamma(E)$ [7]:

$$\Phi(E) \propto E^{-\gamma(E)}, \tag{1}$$

$$\gamma(E) \approx \begin{cases} 2.7, & \sim 10\,\mathrm{GeV} < E < 4 \cdot 10^6\,\mathrm{GeV} \\ 3.1, & 4 \cdot 10^6\,\mathrm{GeV} < E < 10^8\,\mathrm{GeV} \\ 3.3, & 10^8\,\mathrm{GeV} < E < 4 \cdot 10^9\,\mathrm{GeV} \\ 2.7, & 4 \cdot 10^9\,\mathrm{GeV} < E < 3 \cdot 10^{11}\,\mathrm{GeV} \end{cases} \tag{2}$$

These three transition points, where the spectral index changes its value, causing a change in the gradient, are called knee, second knee and ankle. An explanation of the decreasing flux rate after the first knee is that the galactic sources of the cosmic rays cannot contain high energy particles. With a galactic magnetic field B of $10^{-10}\,\mathrm{T}$ and a gyroradius ρ of $5\,\mathrm{pc}$, particles can be contained within the galaxy with a momenta up to:

$$p[\mathrm{GeV}/c] = 0.3B[\mathrm{T}]\rho[\mathrm{m}] \tag{3}$$

This results that they escape from the Milky Way if their energy exceeds $10^6\,\mathrm{GeV}$, leading to the conclusion that particles after the first knee originate dominantly from extragalatic sources. Another explanation of the decrease in the knee is believed to be that galactic sources like supernova remnants cannot accelerate particles to energies higher than $10^6\,\mathrm{GeV}$, since this energy limit is about the maximum energy produced by supernova explosions. The decrease in flux after the second knee in the all-particle spectrum could be effected by the chemical abundance of iron nuclei in the galaxy around that energy. At energies in the order of $10^{19}\,\mathrm{eV}$ the last feature in the spectrum, the ankle, is visible. It starts the last section of the all-particle spectrum which consists of particles that are assumed to result from extragalactic sources [1, 7]. After that, a cut-off can be found which is defined as Greisen-Zatsepin-Kuzmin (GZK) cut-off.
Many sources of cosmic rays are still unknown and not fully understood. Moreover, the search for these sources is complicated by the fact that the majority of cosmic rays, especially the charged component, cannot be traced back to their origin because charged cosmic rays do not travel in a straight path on their way to the Earth. Instead, they are deflected by interstellar magnetic fields. This problem can be circumvented by analyzing uncharged cosmic particles, such as gamma rays and neutrinos. They are unaffected by the interstellar magnetic fields which means their trajectory can be reconstructed and their origin extrapolated.[1]

2.2 Production mechanism of Cosmic Rays

The electromagnetic radiation consists of different ranges classified by their wavelength: radio, infra-red, optical, ultraviolet, X-ray and the gamma ray range. The range of gamma rays is differentiated from X-rays due to their production process, since X-rays are produced in electron transitions in the outer atomic shell and gamma rays are emitted

due to transformations of the atomic nucleus. As a result, there exists a distinguishable classification of the two according to their energy, since energy of the photon depends on its wavelength. As seen in figure 2, the energy range of gamma rays starts at a 10^{-6} eV and ends at 10^{14} eV.

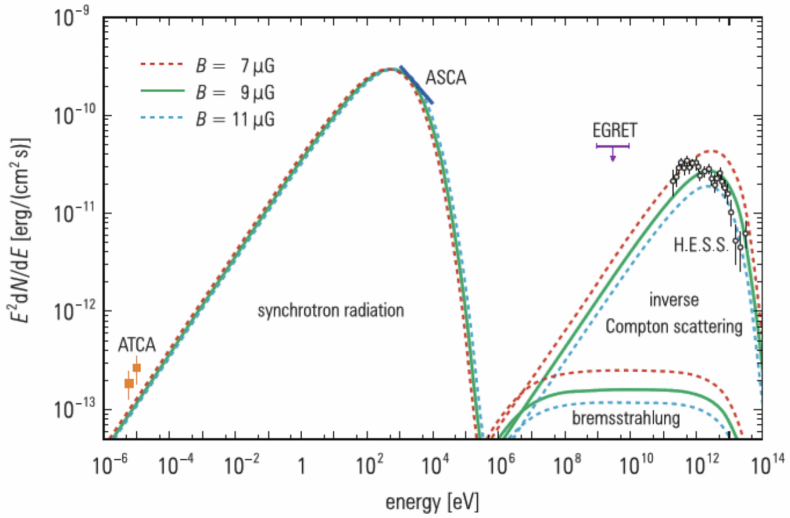

Figure 2: The gamma ray spectrum with the different production processes. Data is taken from ATCA (Australien telescope compact array), ASCA (Advanced satellite for cosmology and astrophysics), H.E.S.S. and EGRET (Energetic gamma ray experiment telescope), which sets an upper limit of the energy spectrum (from [1])

There are a few known sources, which can produce such high energy photons, like supernovae, pulsars, neutrons stars, active galactic nuclei and black holes, which accrete matter. This section will focus on the different production mechanisms of gamma rays, which are the Synchroton radiation, the Bremsstrahlung, the Inverse Compton Scattering and the Neutral pion decay.

Synchroton radiation and Bremsstrahlung

When a charged particle moves along the magnetic field lines, it propagates in a spiral motion and is accelerated in the process. Due to this motion, the charged particle emits Synchrotron radiation [1]. This effect is shown in figure 3. The magnetic field of the source and the energy spectrum of the electron influences the shape, the absolute height of the emission spectrum and also the radiated power P:

$$P \sim E^2 B^2 \,, \tag{4}$$

where E is the energy of the electron and B is the magnetic field. In figure 2 it can be seen that the contribution of Synchrotron radiation dominates up to energies in the order of 10^5 eV in the gamma ray spectrum.

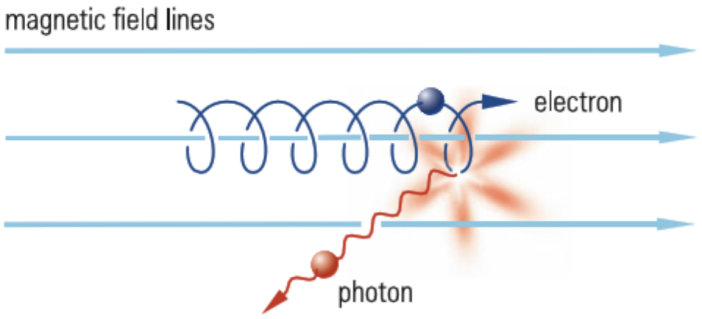

Figure 3: Illustration of synchrotron radiation production with a moving charged particle in a magnetic field (figure taken from [1])

If a charged particle extends the its kinetic energy over 10^6 eV, it is deflected in the coulomb field of another charged particle during an interaction with matter. As that, the accelerated particle experiences a loss of energy due to the emission of a radiation called Bremsstrahlung (seen in figure 4). This energy loss of an electron can be calculated by using

$$\frac{dE_e}{dx} = \frac{4nZ^2\alpha^3(\hbar c)^2 E_e}{m_e^2 c^4} \cdot \ln \frac{a(E)}{Z^{-3}} \tag{5}$$

where

- E_e the kinetic energy of the electron,
- c the speed of light,
- n the particle density,
- Z the charge of the interacting nuclei,
- distance a between electron and atomic nuclei which is necessary to still allow the deflection and
- the fine structure constant $\alpha = \frac{e^2}{4\pi\epsilon_0\hbar c}$.

A characteristic length is the radiation length X_0 defined as length after which energy of the electrons decreases to $1/e$ of its original value:

$$X_0 = \left(\frac{4nZ^2\alpha^3(\hbar c)^2}{m_e^2 c^4} \cdot \ln \frac{a(E)}{Z^{-3}} \right)^{-1} \tag{6}$$

The energy range in which Bremsstrahlung adds to the gamma ray energy spectrum extends from about 1 MeV to about 10 TeV (see Figure 2) [1].

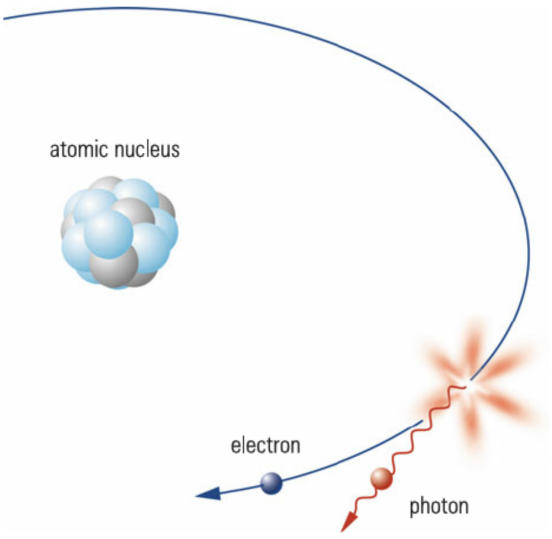

Figure 4: An illustration of the emission of Bremsstrahlung by refraction of an electron in the Coulomb field of a atomic nucleus (figure taken from [1])

Inverse Compton Scattering

Gamma rays can also be produced by Inverse Compton Scattering which contributes to the gamma ray spectrum in an energy range between 1 MeV and 100 TeV. In this process, due to the collision of a low-energy photon a high-energy electron (illustrated in Figure 5) the electron transfers some of its energy to the photon. These low energy photons often originate from the Cosmic Microwave Background (CMB) or starlight. As a result, a lower energy electron and a higher energy photon are created [1].

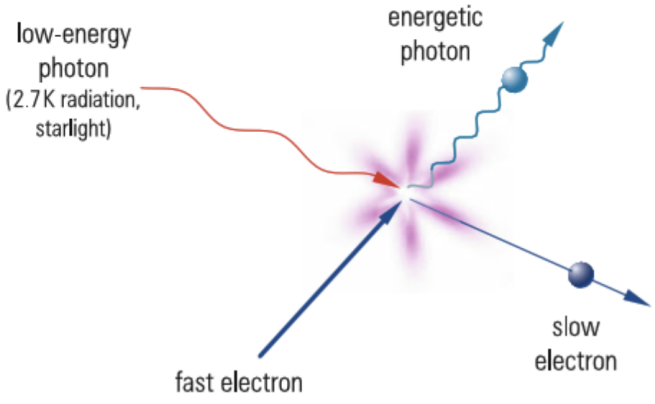

Figure 5: Schematic view of the Inverse Compton Scattering process. (figure taken from [1])

Neutral pion decay

During a proton-proton collision or a proton-nucleus collision, a high accelerated pion can produce charged pions π^+ and π^- and neutral pions π^0 with equal probability. The emission of gamma radiation occurs due to the decay of π^0. As Figure 6 illustrates, the production of two photons can be described as

$$p + \text{nucleus} \longrightarrow p' + \text{nucleus}' + \pi^+ + \pi^- + \pi^0$$

and

$$\pi^0 \longrightarrow 2\gamma$$

The energy of the produced gamma rays depends on whether either the pion decays in motion or at rest. When it decays at rest, both photons have the same energy, which is half the rest mass of the pion $m_{\pi^0} = 135\,\text{MeV}$. Otherwise, the energy of the two gamma rays differ from each other [1].

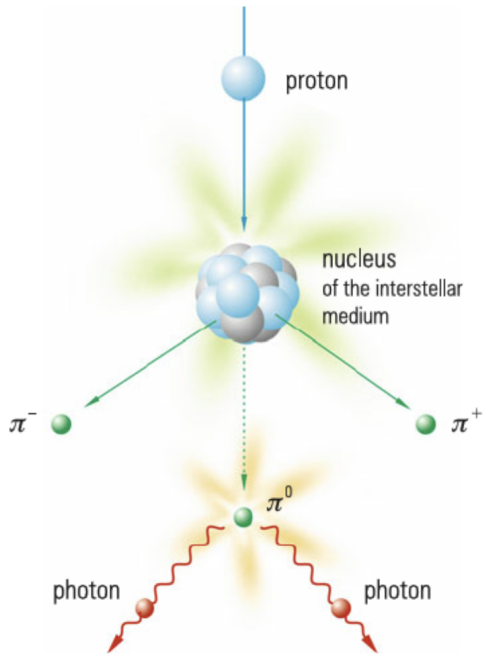

Figure 6: Neutral pion, produced in proton-proton or proton-nucleon-interactions, decays into two photons with the same energy (figure taken from [1])

3 Detection of gamma rays

The incoming flux is lower for photons with higher energy than for photons with lower energy. Therefore, the required detection range depends on the energy of the photon. There are two ways to detect CR depending on the energy of the photon: either directly or indirectly. Direct measurements, e.g. with calorimeters, provide information about the energy and momentum of the particle absorbed by the detector. Since cosmic rays cannot propagate through our atmosphere without interacting with it, space-based telescopes such as Fermi-LAT are used for direct measurements. They require a very large coverage area for measuring very energetic gamma rays for adequate statistics, since the event rate decreases with the increasing energy of the primary particle. Therefore, ground-based telescopes are used for measuring indirectly such high-energetic particles [1]. In the following chapter the interaction processes of primary cosmic rays entering the atmosphere are explained and their detection is explained.

3.1 Extensive air showers

When cosmic rays and gamma rays enter the Earth's atmosphere, they cannot penetrate it without interacting with the atomic nuclei in the air. This creates more secondary particles, which in turn can create even more particles. A particle cascade is created which is called particle shower or Extensive Air Shower (EAS). Because of the very energetic particles, Cherenkov light is emitted as they travel faster than the local speed of light. This radiation can be measured with instruments on the ground. Particle showers can be divided into two categories depending on the primary particles: electromagnetic or hadronic [1].

Electromagnetic showers

If the primary particle is an electron, positron or photon, an electromagnetic cascade of such particles is created, since they interact only via the electromagnetic force. The main processes occurring are Bremsstrahlung, which was explained in the previous chapter 2.2, and pair production. In pair production, an electron-positron pair is be created when a photon with an energy more than twice its rest mass is near another nucleus. The electromagnetic cascade is a repetition of the two processes. The number of particles in such a shower increases exponentially until the energy of the particles fall below a certain critical energy E_c. Above this limit, ionization becomes the dominant process by which the particles loose energy. So the particle shower stops.

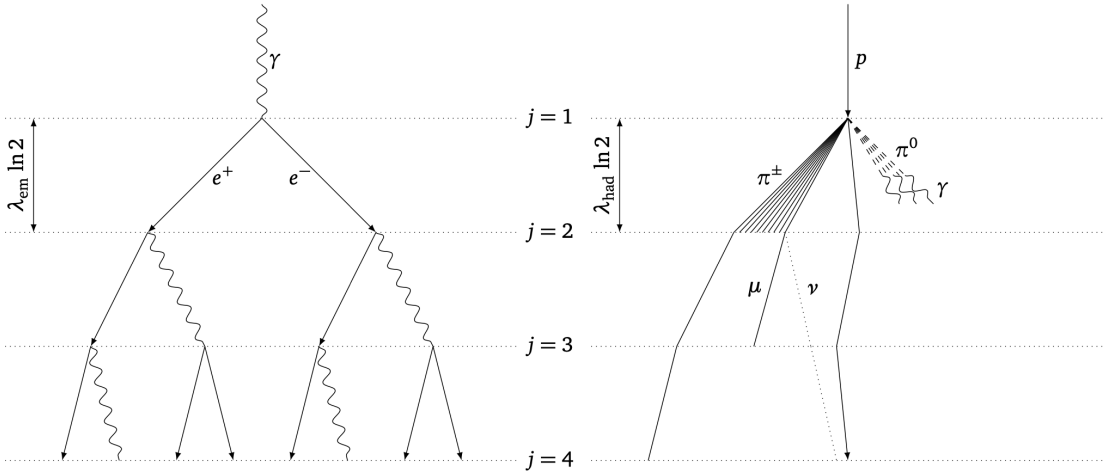

Figure 7: Simplified illustration of extensive air showers. On the left side, primary particle, a photon, decays into an electron-position pair (figure taken from [4])

A simple description of such particle shower formation was first developed by Bethe and Heitler [8] and is shown in Figure 7 (left) for a primary photon generating the electromagnetic cascade. From the previous chapter, we know that in Bremsstrahlung, the radiation is usually equivalent to the distance at which the lepton loses $1/e$ of its energy. In pair production, however, this coincides with the mean free path length of a photon. After each step, the energy of the primary particle is divided equally among the new formed particles. The number of particles after each step n of the shower can be calculated by

$$\mathrm{N} = 2\mathrm{n} = e^{x/X_0} \tag{7}$$

and the shower depth is defined as:

$$x = \mathrm{n} X_0 \ln 2 \tag{8}$$

The maximum shower depth X_{max} can be calculated using

$$X_{max} = X_0 \frac{\ln E_0/E_c}{\ln 2} \tag{9}$$

The first particle interactions and EAS shower formations already occur at around $15\,\mathrm{km} - 20\,\mathrm{km}$ above sea level, because the radiation length of photon and electrons in air is much smaller then atmospheric column density.

Hadronic showers

Hadronic showers, however, are more complex than electromagnetic ones because of the strong and weak interactions. When protons enter the atmosphere, proton-proton or proton-nucleus interactions occur, producing pions and kaons (see figure 7 right). At this

stage, pionization occurs, producing more pions due to pion-nucleus interactions. This process is stopped when their energy falls below the critical energy, so the pions decay rather than produce new particles. From section 2.2, a neutral pion π^0 decays into two photons. These photons can generate electromagnetic showers as described above. In contrast, charged pions decay via the following decay channels:

$$\pi^+ \to \mu^+ + \nu_\mu \text{ and } \pi^- \to \mu^- + \bar{\nu}_\mu$$

The produced muons and anti muon which interact strongly and only lose energy due to ionization decay into:

$$\mu^+ \to e^+ + \nu_\mu + \bar{\nu}_e \text{ and } \mu^- \to e^- + \bar{\nu}_\mu + \nu_e$$

Another major difference between hadronic and electromagnetic showers is their lateral distribution. The different distributions of the two types of showers can be seen in Figure 8. Hadronic showers have a larger lateral extent and are more irregular in shape than electromagnetic showers because of strong interactions producing more lateral momentum as well as more different particles [1, 9].

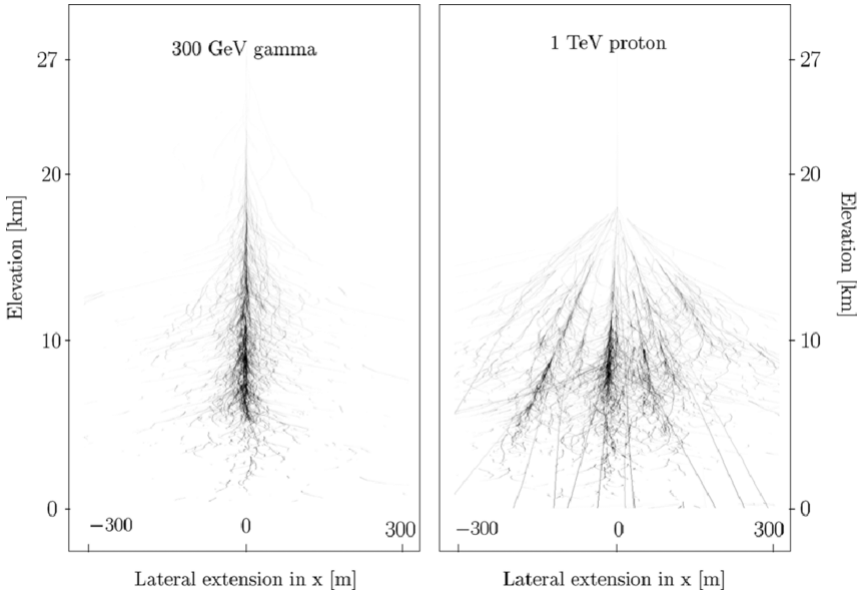

Figure 8: Side-by-side comparison between an electromagnetic shower and a hadronic shower [10]

3.2 The Emission of Cherenkov Light

After entering the atmosphere, air showers develop from the cosmic rays. Particle showers in the range of a few TeV, however, usually do not reach the ground where the IACTs are positioned. Consequently, they cannot be detected directly. Instead, they can be detected

indirectly by measuring the Cherenkov light emission from these particles.
When a charged particle moves faster than the local speed of light of the surrounding medium, Cherenkov light is emitted. For emission of Cherenkov light this condition needs to be fulfilled:

$$v \geq nc\,, \tag{10}$$

where v is the velocity of the particle, c the speed of light and n the refractive index of the medium through which the particle is propagating. Additionally, the Cherenkov light is emitted in a cone-like form with the opening angle θ_{cone} defined as

$$\theta_{\text{cone}} = \arccos\Big(\frac{c}{nv}\Big)\,. \tag{11}$$

During propagation through the medium, polarization occurs. When the particle velocity exceeds the phase velocity of the light in the medium and therefore fullfills the condition 10, the already polarized atoms emit coherent radiation (as it is seen in figure 9). For slower particle velocities than the phase velocity of light in the medium, no Cherenkov radiation is produced because the dipoles cancel each other out [11].

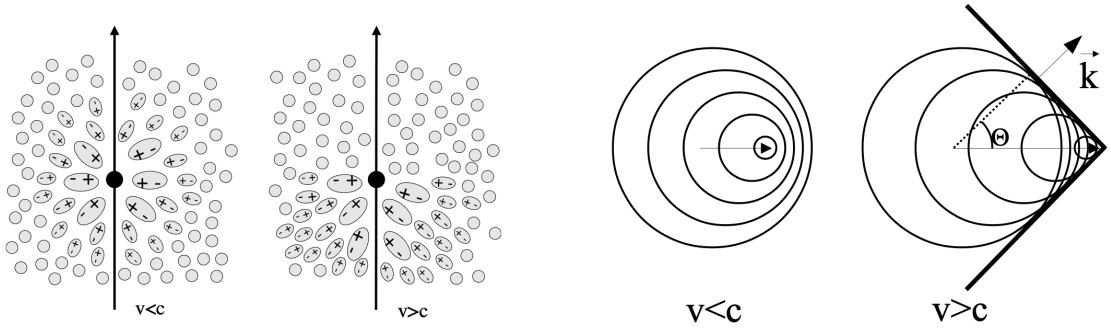

Figure 9: The polarization of the medium induced by the crossing of a relativistic particle (left) and the formation of wavefront of the Cherenkov radiation (right) (taken from [12])

3.3 Detection principle of Imaging Atmospheric Cherenkov Telescopes

Imaging Atmospheric Cherenkov Telescopes (IACTs) use the Earth's atmosphere as their detector medium and with the detection of the Cherenkov light from particle showers they reconstruct the position of the entrance of the primary CR as well as its energy. Figure 10 illustrates the working principle of ground-based telescopes. Due to the enormous extent of the Cherenkov light pool on the ground, the effective range over which the telescopes can detect a shower is quite large. By using large mirror surfaces, the telescopes collect the Cherenkov light and focus it on the camera, which processes the Cherenkov light signal with photon detectors. The resulting images follow an ellipsoidal shape that resembles the shape of the particle shower [12, 14]. Ground-based detectors using this technique

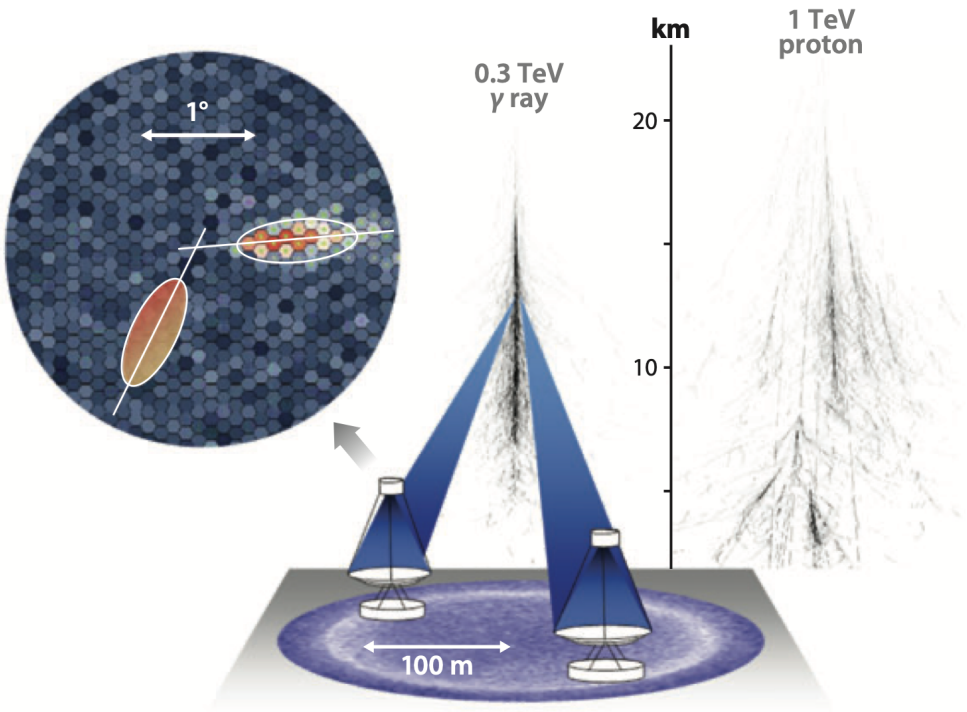

Figure 10: Illustration of the detection technique of IACTs of a electromagnetic cascade produced by a primary gamma ray. The air showers which emit Cherenkov light illuminates an area on the ground. The light is reflected by their mirrors to the camera, only if the telescope is within the illuminated area. (figure taken from [13])

include, for example, the H.E.S.S. in Namibia, the Very Energetic Radiation Imaging Telescope Array System (VERITAS) in the United States, and the Major Atmospheric Gamma Imaging Cherenkov (MAGIC) telescopes on La Palma and the planned Cherenkov Telescope Array, which will be described in the following.

4 The Cherenkov Telescope Array (CTA)

The next generation of IACTs includes the planned CTA, designed to detect gamma rays in the energy range from 20 GeV to 300 TeV. Thus, this array will reach new energy regions which were previously inaccessible to IACTs. In addition, CTA will also be up to an order of magnitude more sensitive than experiments such as MAGIC, H.E.S.S., and VERITAS. For full sky coverage one site will be established on La Palma and another in Paranal Chile in order to cover both hemispheres. Due to the CR flux rate, a large detection area is needed for a sufficient event rate of high energy showers [15]. Figure 11 shows the proposed layouts for both sides.

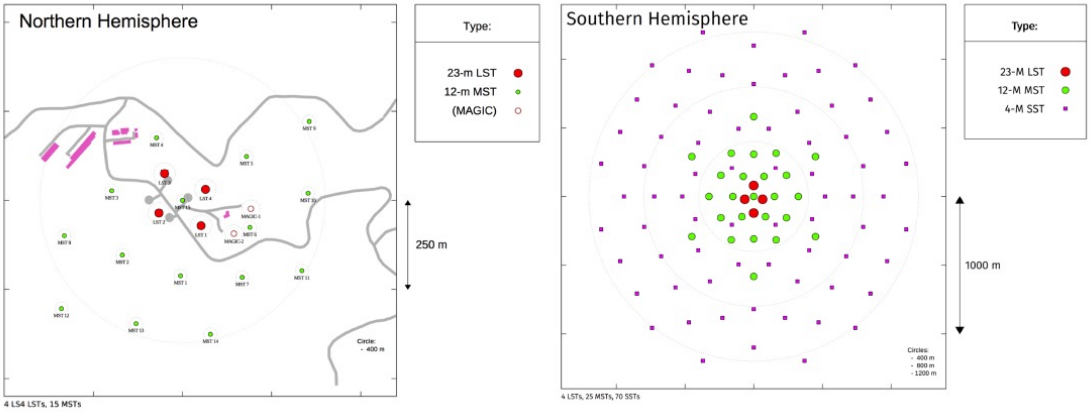

Figure 11: Preliminary layouts for CTA North and South [16]

Due to the intensity of the Cherenkov photons, the different types of telescopes are planned which vary in the size of the photon collection areas. That means that the lower the initial energy of the gamma rays, the larger the photon collection area of the telescope. CTA consists of three different types of telescopes specialized for specific gamma-ray energy ranges:

- **The Large-Sized Telescope (LST)** is specialized in the detection of CR in the energy range from 20 GeV to 150 GeV. A parabolic mirror surface with a dish size of 23 m and a focal length of 28 m is used, resulting in a field of view of 4.3 deg. The LST camera consists of 265 photomultiplier tubes (PMT).

- **The Medium-Sized Telescope (MST)** working energy range is from 150 GeV to 5 TeV and its field of view is ≈ 7.6 deg. The setup of the telescope is in a modified Davies-Cotton design which has a dish size of 11.5 m and a focal length of 16 m. For the MST two cameras, the FlashCam and the NectarCam, are planned to be used on the PMT basis, resulting in a pixel size for both cameras in 0.17 deg. To be mentioned, another design is also proposed for the mid sized telescope, which is the

Schwarzschild-Couder Telescope (SCT) with a primary mirror of 9.7 m, a secondary mirror of 5.4 m and a camera using silicon photonmultipliers (SiPMs). This telescope design has the same field of view as MST, but has a smaller effective area of 41 m^2 for a smaller point spread function. The resulting pixel size of the SCT camera is around 0.067 deg.

- **The Small-Sized Telescope (SST)** works in the higher energy range of CTA (5 TeV to 300 TeV) and initially three different telescope designs (ASTRI-Horn, the GTC and SST-1M) were proposed. However, the CTA observatory then decided on the ASTRI telescope based on the experiences of the previous designs. The diameter of primary mirror is 4.3 m and the diameter of the secondary is 1.8 m and a focal length of 2.15 m resulting in a field of view of 10.5 deg. The SST is equipped with a camera based on the CHEC-S design. The SST camera has in total 2048 SiPMs. Each SiPM tile consists of 256 pixels (area of 3x3 mm^2). Four pixels are connected to a superpixel, which results in 64 pixels for each SiPM tile. With 32 of such SiPMs, the camera has a total of 2048 pixels. Figure 12 shows the SST camera.

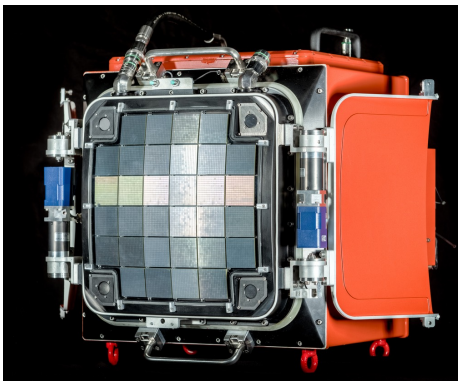

Figure 12: The prototype camera CHEC-S used for SST (picture taken from [17])

The different telescope types are illustrated in figure 13. On the north hemisphere, four LST and 15 MSTs are planned. Four LST, 25 MSTs and 70 SSTs are planned to be built on the south hemisphere [15, 16].

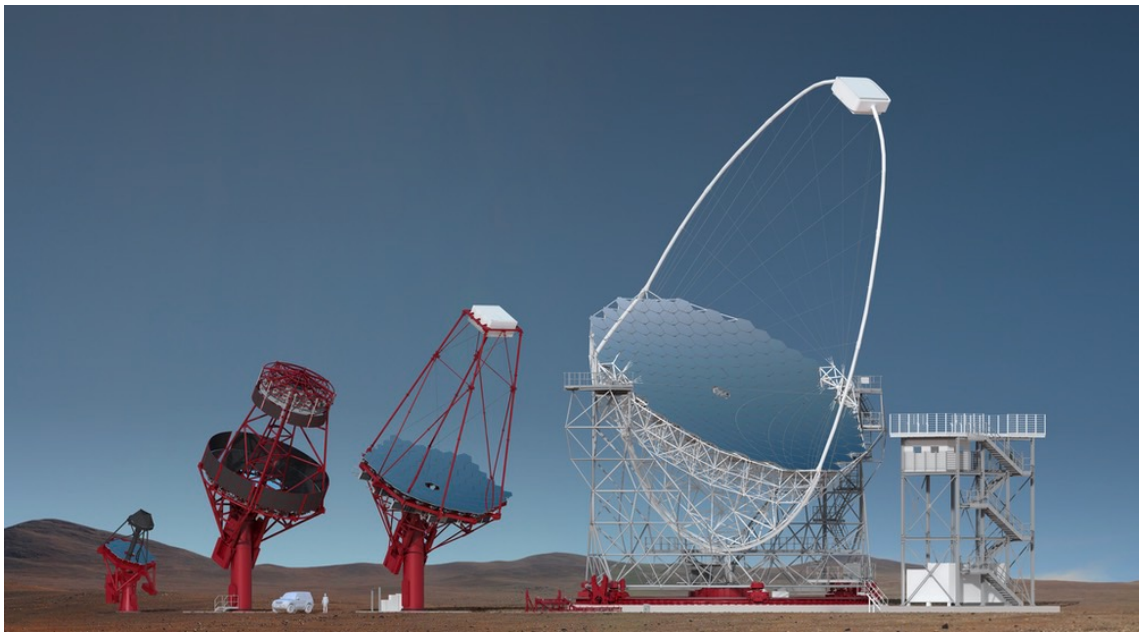

Figure 13: Visualization of the SST, the two mid sized telescopes SCT and MST and LST (from left to right)[16]

5 The DesertACT telescope

As part of the Gen2 upgrade an extention of the IceTop array is planed. A candidate for the extension is the IceACT project. It features many small and cost effective IACTs to cover a large area. IceCube includes an the array on the surface to serve as a partial veto for the down-going background of penetrating muons created by cosmic-ray interactions in the atmosphere above the detector.
To validate the performance, the Namibia campaign was launched in collaboration with H.E.S.S. The IceAct telescope used during this campaign is assigned the name DesertACT (DACT). The following section will describe the simulation of the air showers and detector response of DACT.

5.1 Simulation of air showers and the detector response of DACT

For the simulation of DesertACT, two common programs are used: CORSIKA (COsmic Ray SImulations for KAscade v7.6900) and sim_telarray [18]. CORSIKA generates atmospheric air showers using the Monte Carlo (MC) method. More information about the different shower models can be found in [18]. The gammas and protons of the cosmic rays are produced in energy range between 500 GeV to 10 PeV with a spectral index of -1.5 and a zenith angle of 30 deg. Additionally, the protons are simulated as diffuse shower with a viewcone opening angle of 15 deg, whereas the gammas as point source. The spectral index is chosen in order to reduce the simulation time on the one hand and to obtain good statistics on the other for each energy range. In the data analysis, the spectrum is reweighted with a function of the python package pyirf [19] which uses the following formula:

$$\omega_i = \frac{\Phi_{\text{Target}}(E_i)}{\Phi_{\text{Simulation}}(E_i)} \tag{12}$$

with $\Phi_{\text{Target}}(E_i)$ being the true flux with a spectral index of -2.7 and $\Phi_{\text{Simulation}}(E_i)$ the simulated one. As location for the simulation the location of H.E.S.S. was decided. Each simulated shower is used 25 times on a circular area with a radius of 1500 m.
The generated Cherenkov photons of the atmospheric air showers are forwarded to sim_telarray, in which the detector response is simulated. The detector is defined by a multitude of parameters that control aspects of the telescope optics as well as its electronics. For the detector response of DACT an already existing telescope was used [20]. The position of the telescope is decided to be the origin of the coordinate system and the used telescope radius is 60 cm. The following section describes the setup of the DACT telescope and its camera. For more detailed description of the implementation of the telescope is found in [20].

5.2 Setup of the telescope

Fig. 14 shows the components of the DACT telescope. The basic frame of the telescope is a lens tube made of carbon fibre with a height of $\approx 55\,\text{cm}$. Cherenkov light is collected by a fresnel lens with a diameter of 60 cm and gets focused on the camera plane. This Fresnel lens is embedded in a plastic ring and covered by a glass plate. Since this telescope is is usually operated at arctic temperatures, the inside of the plastic ring is heated by a heating cable so that there is no moisture on the glass. At the bottom of the telescope is a circular hole for the upward-facing camera and a solid aluminium housing that contains the control and readout electronics.

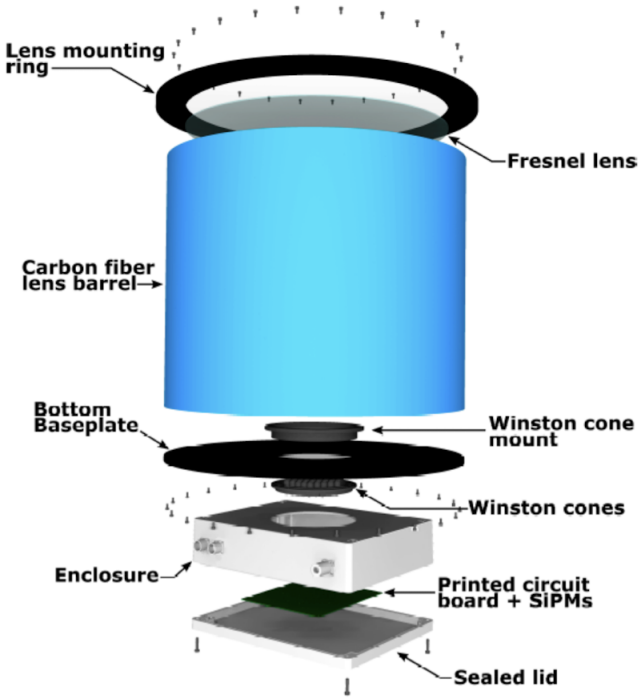

Figure 14: A schematic sketch of the setup of the telescope. On top of the Carbon fiber lens barrel sits a fresnel lense ($\approx 55\,\text{cm}$ diameter), focusing the incoming light through the tube on to the camera. Underneath the camera, which consists of the SiPMs with the Winston cones, are the readout electronics, protected by solid aluminium housing.

The camera, as it is seen in Fig. 16, consists of 64 Silicon Photomultipliers (SiPMs) with TARGET (TeV Array Readout Electronics with GSa/s sampling and Event Trigger) Readout Electronics. Before the photons hit the SiPMs, they get collected by Winston cones (as seen in Fig. 15). The great advantage of Winston cones is that their material and shape is chosen in such a way that all incoming photons are totally reflected at the side surface, regardless of the angle of incidence of the light. Since the entire telescope has

a total weight of less than 20 kg, it can be mounted on a standard telescope mount. This enables star tracking capabilities for the telescope [4, 21].

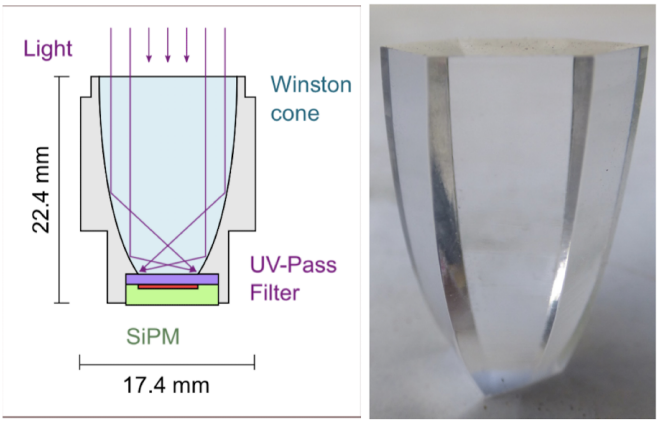

Figure 15: Sketch and a close-up photo of a Winston cone. First, the Cherenkov photons hit the hexagonal shaped surface, travel through the cone and get reflected to the squared shaped bottom, before they reach the SiPMs.

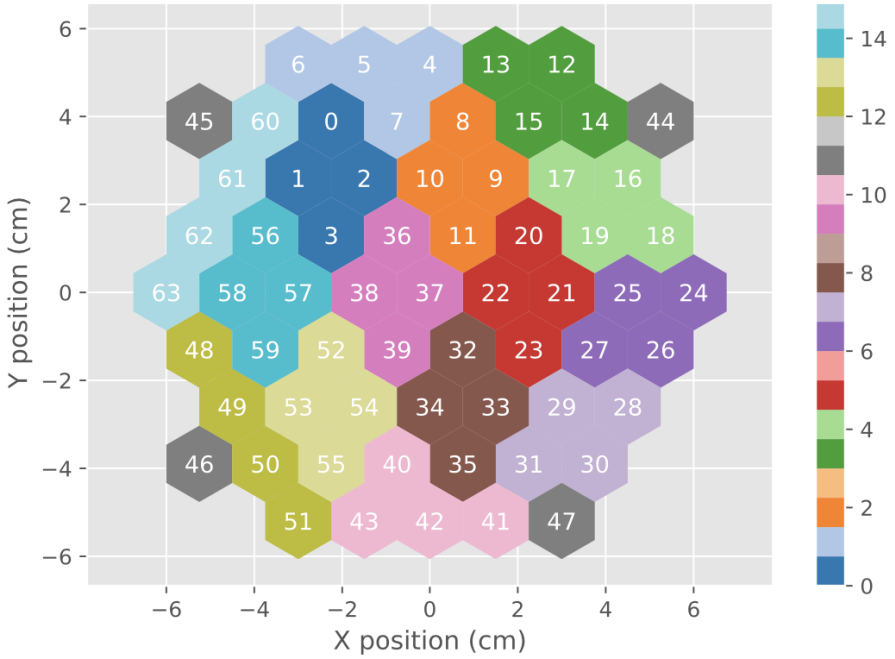

Figure 16: Camera layout of DesertAct as implemented in *sim_telearray*. The 64 pixels are grouped in trigger groups (each group consists of four pixels which are grouped in colours)

5.3 Data analysis of DesertAct

When the full simulation is finished, the data can be analyzed. To extract only the information of the particle shower, some prior steps need to be taken. Since the shower images in the detector are overlapped with fluctuations of the night sky background and the electronics response, an image cleaning and some precuts helping to remove insufficient images are performed. The steps for this processed are summarized in the following:

- **The Camera position cut** ignores all images having their maximum signal pixel outside the circle, whose radius is 5 cm and whose centre is in the centre of the camera (like shown in Fig. 17).
- **In Multiplicity cut**, only images will succeed, if at least one pixel has a threshold over 200 Analog-to-Digital-Converter count value (short in this thesis ADC, one photoelectron (pe) corresponds to 6 ADC [22]). This cut is convenient for an easier image cleaning process.
- **Tailcuts cut** function from the ctapipe package of the CTA Collaboration [23] consist of three different parameters (picture threshold, boundary threshold and the minimum number of picture neighbors):
  - Picture threshold (set here at 200 ADC) is a threshold value above which all pixels are kept.
  - The Boundary threshold is minimum value above which all pixels are maintained if the neighbor pixel are above the picture threshold. In this data analysis, the value decided at 40% of the picture threshold.
  - The minimum number of picture neighbors is fixed at two. This means that an image pixel only survives if it has at least two triggered neighbor pixels.

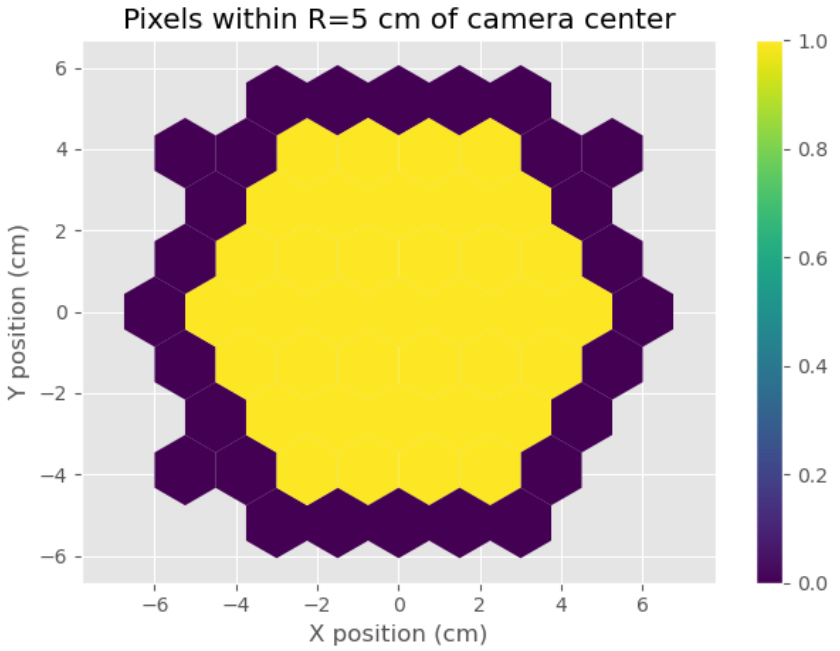

Figure 17: Illustration of the Camera position cut on the IceAct camera. Only events with their maximum signal pixel inside the yellow region survive this cleaning step.

With the cleaned image the showers information can be extracted by a hillas parameterization, also called as hillas analysis. In the hillas analysis, first proposed by A. M. Hillas [24], the shower pattern is approximated by an ellipse. With the help of the simplified elliptical shape, image properties such as

- the image amplitude which is the sum of all pixels in the hillas ellipse,
- width and length of the ellipse,
- the distance r between the camera center and the center of gravity of the shower and
- angle ϕ being the orientation of the image in the camera plane

can be extracted.

5.4 Gamma-Hadron-separation with DesertACT

The idea is to perform an event reconstruction with an array of DACT telescopes. Hence the question arises, if it is even possible with one telescope to distinguish gamma showers and hadron showers. A simple and quick method is to compare the widths and lengths extracted from the Hillas analysis between gammas and protons. The width and the

length parameter of the shower differ from each other because gamma showers have a much slimmer profile than protons (see section 3.1).
The table 1 shows the percentage of incoming gamma and proton events that successfully pass each precut step.

	Gamma	Proton
Total number before precuts	153417	41319
Camera position cut	90.96%	61.32%
Multiplicity cut	64.07%	56.14%
Tailcuts and Hillas extraction	75.83%	76.23%
Total number after precuts	68156	10785

Table 1: Percentage of survived Events after each precut. After all precuts, around 44.43% of gamma events and 26.1% of proton events survived

To be mentioned, not every cleaned image can survive a hillas analysis due to its relatively small size in the camera. As a result, the extraction of width and length is successful for 44 % of gamma and 26 % of hadron showers. The width and length distribution of both particles is shown in figure 18. One can clearly see that both distributions are not easily separated. Hence, a distinction between hadron showers and gamma showers is not possible with the Hillas parameterization because of the current setup of the telescope. To find an explanation why the setup limits the separation power, the field of view in DACT is compared to the field of view from H.E.S.S. (5 deg), performing a good gamma-hadron-separation.

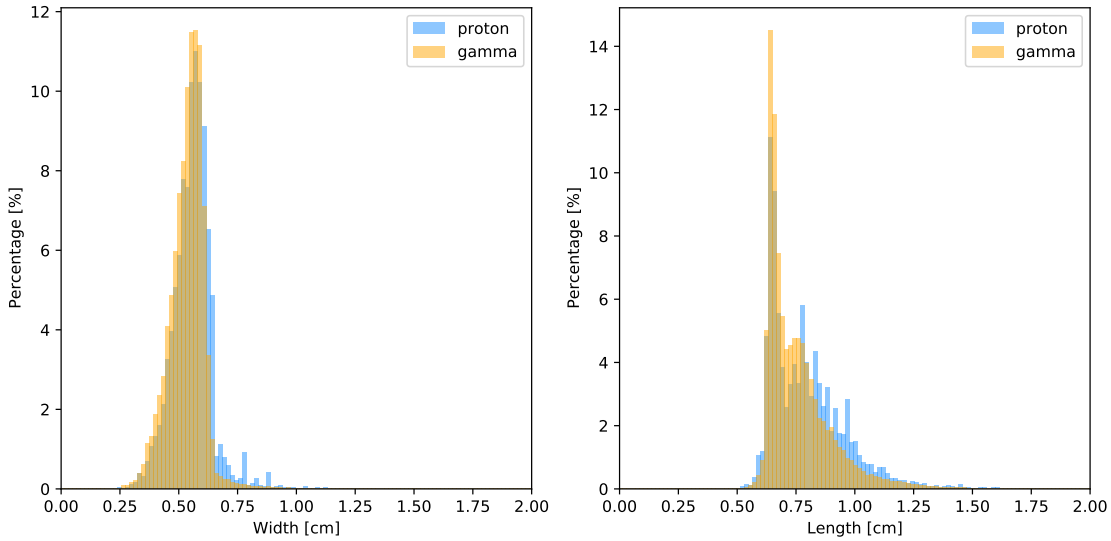

Figure 18: Hillas width and length of triggered gamma and proton events in DACT.

Figure 19 shows a 2.6 TeV proton shower and 1 TeV gamma shower, both simulated in H.E.S.S., in the camera plane of DACT. From perspective of DACT, both events have approximately the same size in the camera. Therefore, simple classification of gamma events and proton events is not possible. In order to improve the separation of proton showers and gamma showers, the DACT camera would require smaller pixels.

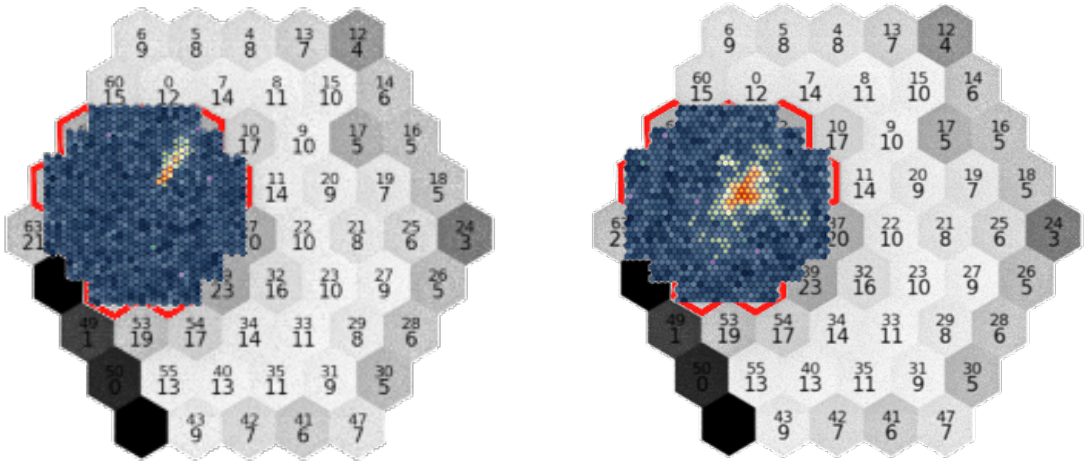

Figure 19: Example events from Hess from the view of DesertAct. The pixels 44, 45 and 46 of DesertAct camera are for simplicity ignored in this sketch. On the left side, a gamma events has been triggered in HESS. On the right side, a proton event is illustrated (event pictures are taken from [9]).

Since the main focus of this work is to realize successful event reconstruction and gamma hadron separation with an IACT on smaller size scales, one can see that the DACT setup is not precise enough. For this reason, a new type of a tiny sized telescope is created and simulated in the following chapter.

6 First performance analysis of a new type of a tiny sized telescope

Nowadays the Schwarzschild-Couder telescope (SCT) design, like the SST of CTA (shown in chapter 4), shows a very good performance in the event reconstruction because of the small effective area for a small point spread function. Therefore, the idea of a meter sized SCT came along.
The aim of this chapter is to create a scaled down version of SST and analyze its performance. The shower simulations of TinyTel have the same CORSIKA parameters as DACT with the exception of the viewcone (15 deg → 6 deg) and the telescope radius (60 cm → 300 cm). In the following section, the setup of TinyTel as it is implemented in sim_telerray is described.

6.1 Setup of tiny-sized-telescope

The optical setup and the camera of TinyTel is described as it follows.

6.1.1 Optical setup

The basic framework is a Schwarzschild-Couder configuration. Table 2 shows the changed optical parameters between TinyTel and SST as they are implemented in sim_telerray in comparison. In general, every used optical parameter from the SST-ASTRI-optics

	SST-ASTRI-CHEC-S	TinyTel
Primary mirror diameter	424.1 cm	178.122 cm
Secondary mirror diameter	180 cm	75.6 cm
Focal length	215 cm	90.3 cm
effective focal length	215.191 cm	90.38 cm
segmentation of primary mirror	hexagonal-shaped panels	None

Table 2: Comparison of optical components between TinyTel and the SST-ASTRI-CHEC-S telescope

configuration is scaled down by a factor of 0.42 for the config-files of the TinyTel telescope resulting in a field of view of 10 deg Additionally, because of the smaller primary mirror having a diameter of ≈ 178 cm, the segmentation which is used in the SST-setup is removed. Figure 20 illustrates in the x-z-plane the mirror alignment of the telescope. Moreover, the camera body and how they are implemented in the SST setup, are removed for our purpose.

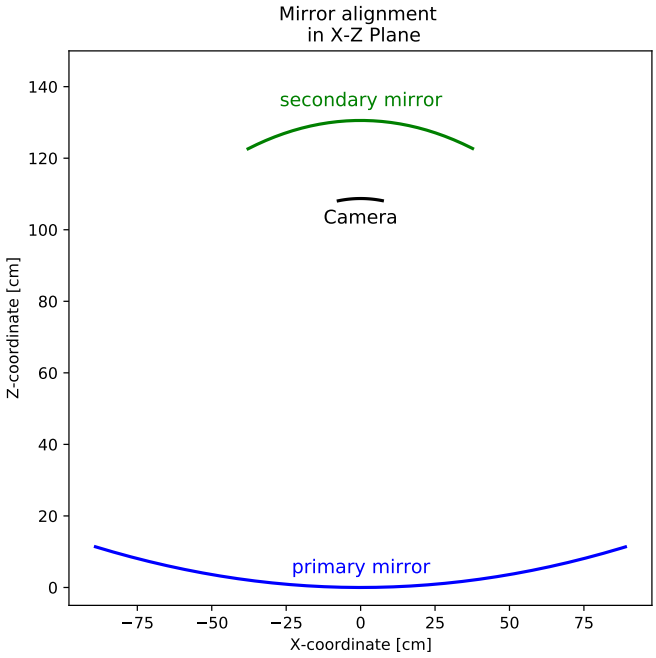

Figure 20: Representation of the optical setup of TinyTel in the x-z-plane.

6.1.2 Camera layout

The camera of the TinyTel telescope is a scaled down version of the CHEC-S camera used in the SST-ASTRI setup, but with a different pixel mapping. The layout of the camera as it is implemented in sim_telerray is shown in 21. In total, the camera consists of 448 pixels which are grouped in 2x2 pairs, so that we get in total 112 pixel modules. The pixel size of the camera is 6 mm. The camera diameter is around 15 cm. The pixel spacing between every pixel is 0.2 mm and the module spacing between each module is 1 mm.

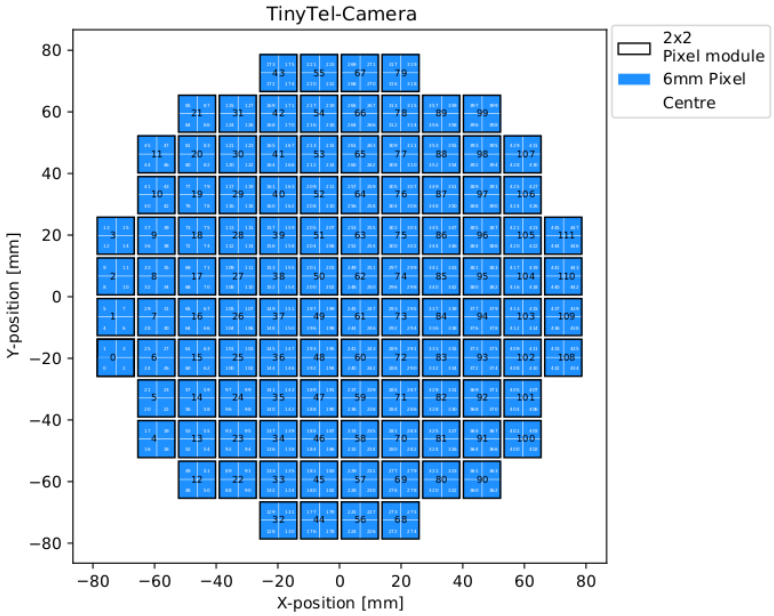

Figure 21: Camera layout of the TinyTel as implemented in sim_telerray.

6.1.3 Validation of optics

After implementing the configuration files for the TinyTel telescope in sim_telerray, the optical system and the camera feedback need to be validated first. Therefore, ray tracing is performed and the point spread function (PSF) as a function of the field angle is characterized in the following section.

Ray tracing

The ray tracing technique is used during design study phases of new telescopes to simulating the optics before building the telescope. Therefore, a huge number of photons is simulated parallel to the optical axis of the telescope. As a result, one would expect a PSF in the center of the camera. The photon distribution on each optical component of the telescope is shown in Figure 22. Figure 23 illustrates the light path of the ray tracing photons. Noticeable feature is the evenly distributed primary mirror. The center of the primary mirror shows the shadowing of the secondary mirror because some photons are reflected to the back side of the secondary mirror. After hitting the primary mirror, the photons get reflected to the secondary mirror (Fig. 22 upper right) before they get focused on the center of the camera. On the secondary mirror the shadowing of the camera plane is seen, because some reflected photons from the primary mirror hit the back of the camera. On the camera plane, we see a focused PSF (Fig. 22 lower left), but in reality in the center of a camera having a module spacing (seen in 16) of 1 mm (red lines).

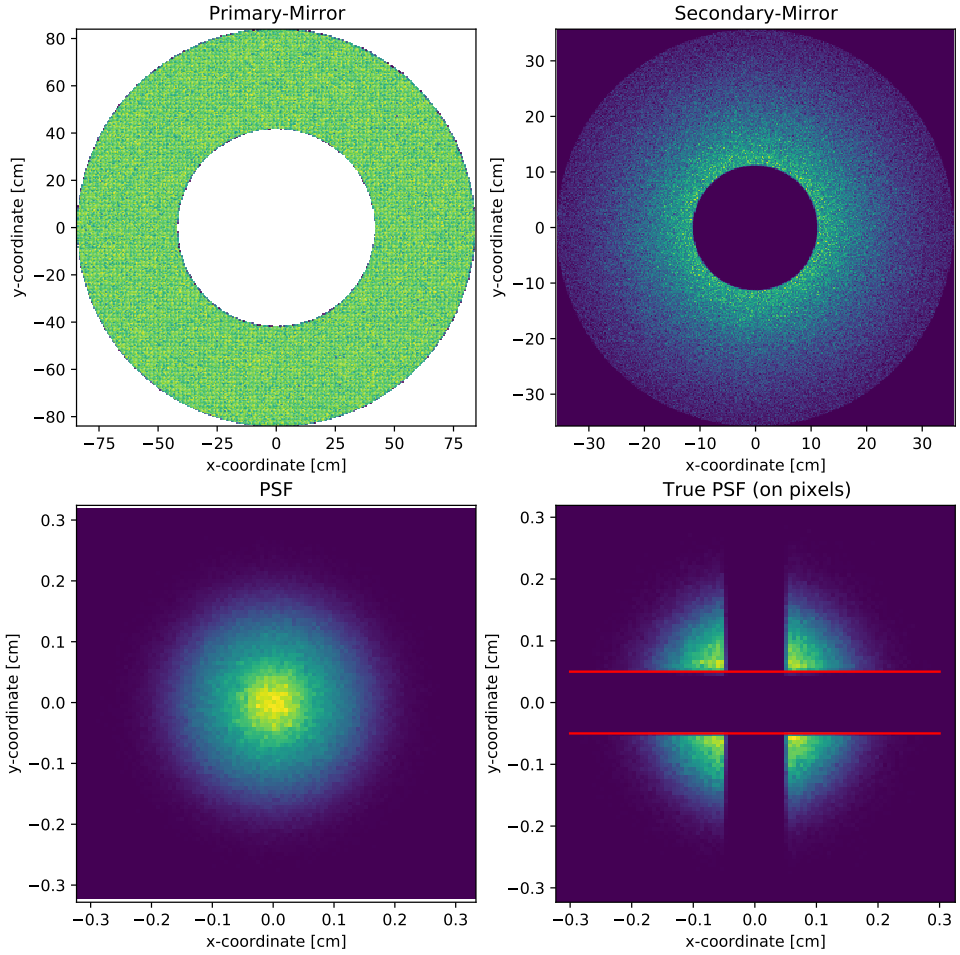

Figure 22: Ray tracing in each optical component plane of TinyTel. The upper row shows the photon distribution on the primary mirror and the secondary mirror. On the bottom row the PSF is shown. On the left side the PSF on the pixel plane and on the right side the PSF with the pixel mask.

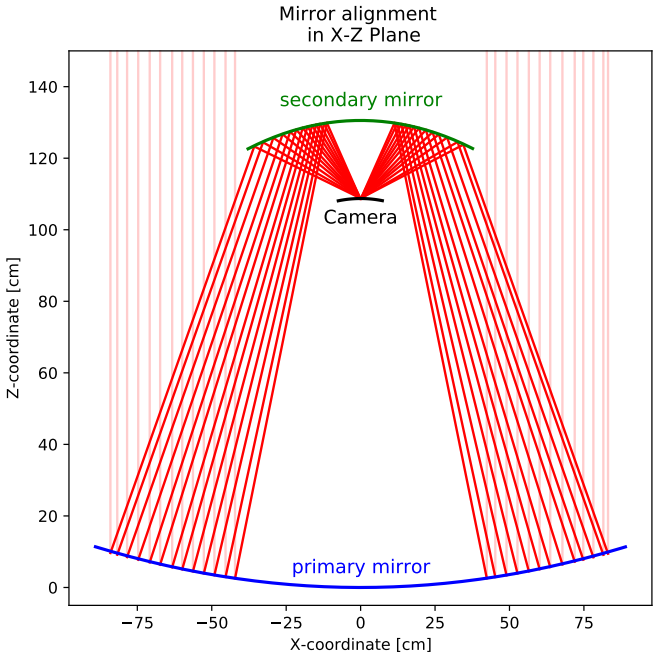

Figure 23: Light path in the x-z-plane of the telescope for parallel light.

PSF-analysis

For analysing the PSF, first of all the detection efficiency defined as the fraction of the number of the detected photons from all simulated photons is determined as a function of the offset angle of the incoming light to the optical axis, which can be seen in Figure 24. It can be seen from the graph that there are small dips in the recorded rate as some photons hit the spacing rather than a pixel. The greater the spacing, the greater the dips. As soon as the camera's field of view is left, the efficiency drops to zero.

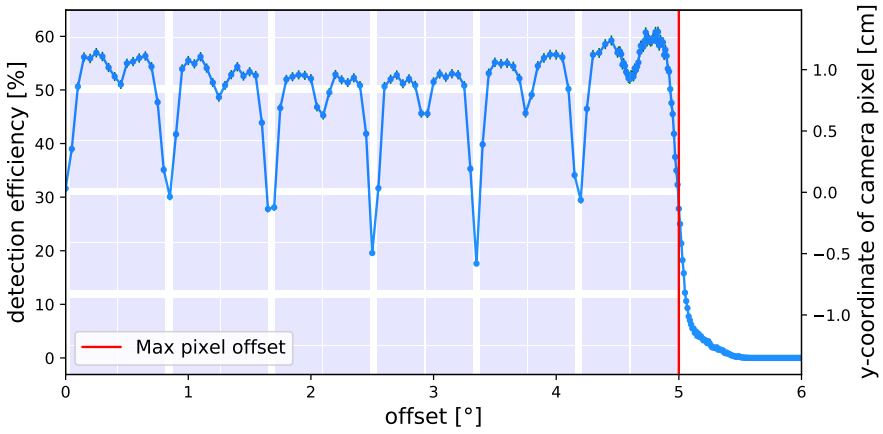

Figure 24: Detection efficency as a function of offset angle of the incoming light to the optical axis with highlighted pixel layout

Since the incoming signal is Gaussian scattered, it is important to capture a large portion of the center of the signal. For this purpose, the containment radius of 90 % of the PSF is determined as a function of the offset angle of the incoming light to the optical axis. From figure 25, we can result that the containment radius of 90 % of the PSF is smaller than a pixel size.

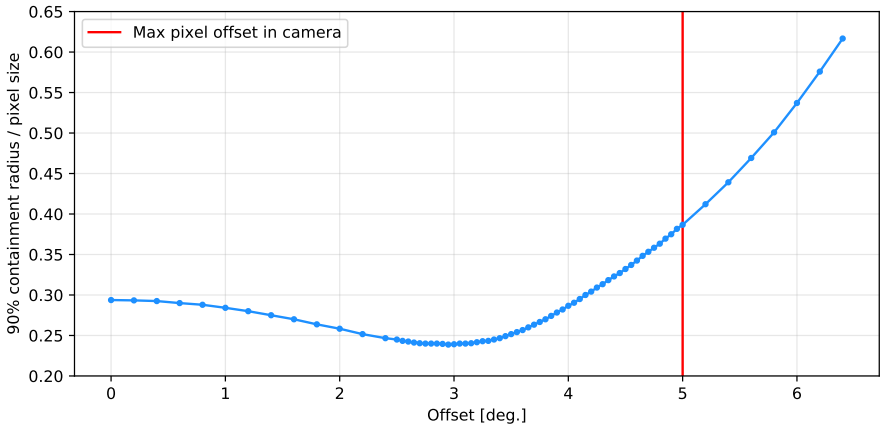

Figure 25: 90 % containment radius of PSF as a function of offset angle of the incoming light to the optical axis in pixel size of TinyTel

6.2 Image cleaning analysis

Before the events are reconstructed, image cleaning is performed. This is necessary to select only the pixels that contain Cherenkov light, since the images contain Night Sky Background (NSB). Therefore, the image size which is the sum of the pixel amplitudes

is reduced. It should be mentioned that the image cleaning also results in a loss of information as low intensity pixels at the edge of the shower region are removed from the image. This has a significant impact on small images, where these cuts result in a smaller image than expected. Since the shower energy is proportional to the determined number of photoelectrons in the image, this leads to more bias of the reconstructed energy [25]. For the image cleaning, tailcut cleaning from the Python package ctapipe [23] is used. For tailcuts cleaning, three different thresholds (see chapter 5.3) need to be specified. In the following sections, one is only concerned with determining the appropriate value for the image threshold and the edge threshold. For simplicity, in the first step of the analysis, preselected events with an image size greater than 10^4 ADC counts (see Fig. 26) were considered first before all events were analyzed. For the last parameter, the default setting was chosen (minimum number of image neighbors = 2). In addition, after the threshold tests, the first hillas analysis for this telescope is performed for all images.

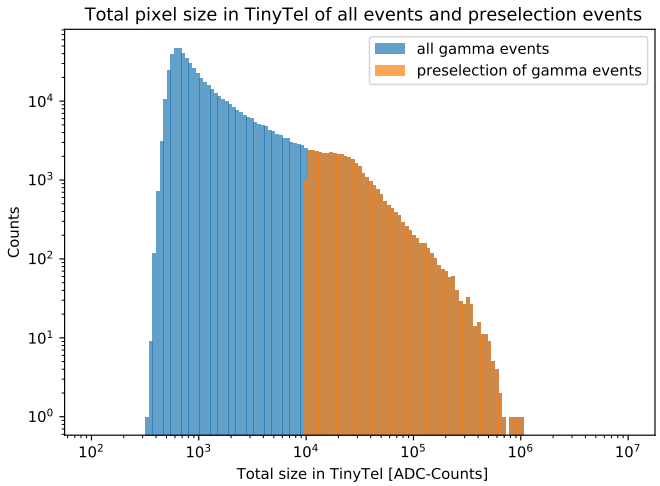

Figure 26: Total pixel size distribution of all simulated gamma events. Events with an image size above 10^4 ADC (orange) are used as a preselection for testing

6.2.1 Boundary threshold

To determine the minimum threshold value above which all pixels are retained when the neighboring pixels are above the screen threshold, the decrease in amplitude from the pixels to the first neighbor is considered. For this purpose, an image threshold is set fixed and defined based on this threshold. Fig. 27 displays the decrease in amplitude from pixels with a picture threshold of 200 ADC counts. From this one can see that there is a large decrease in amplitude over 50 %, meaning that the majority of the camera pixels have low pixel value or are not triggered pixels. Furthermore, negative decrease values give statement that neigbor pixel value is above picture threshold, meaning that the neighbor

pixel is brighter. From the results, the boundary threshold of the tailcuts cleaning is set at 50 % of picture threshold.

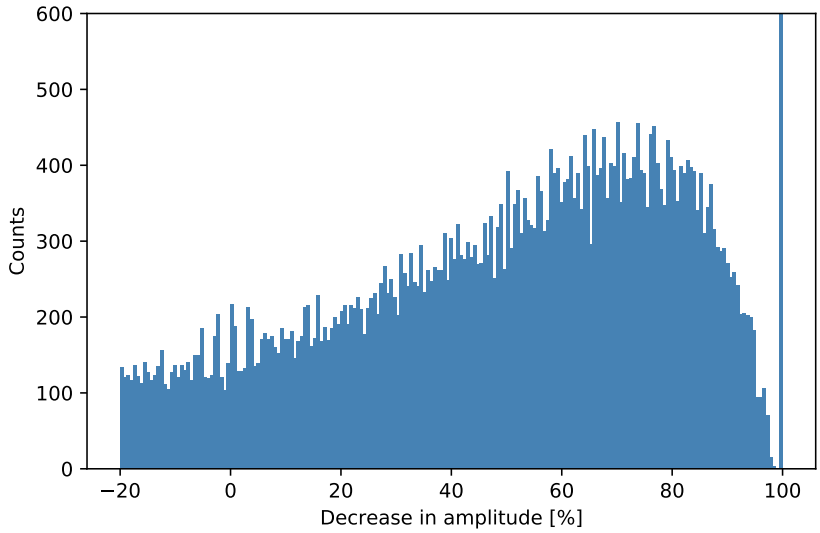

Figure 27: Decrease in amplitude from pixels with 200 ADC-Counts to first neighbour

6.2.2 Picture threshold

For decision of picture threshold, being the value above which all pixels are kept, the average width and length of the shower events are calculated as a function of the picture threshold. When the threshold is set to a small value, we end up with wider images in the camera for Hillas analysis on the one hand, and more NSB fluctuation pixels on the other. This can actually degrade our reconstruction in the end. For this reason, determining this value is very important for the later stages. From Fig. 28, the average width and length of the preselected events begin to decrease at 5 ADC counts. There is a clear difference in average and derivation of width and length for all events between very small picture thresholds and picture threshold above 10 ADC counts. Both distributions become increasingly narrow and the average mean decreases, as the picture threshold rises. Consequently the threshold is set at 10 ADC counts, since above this value there is no significant change in gradient.

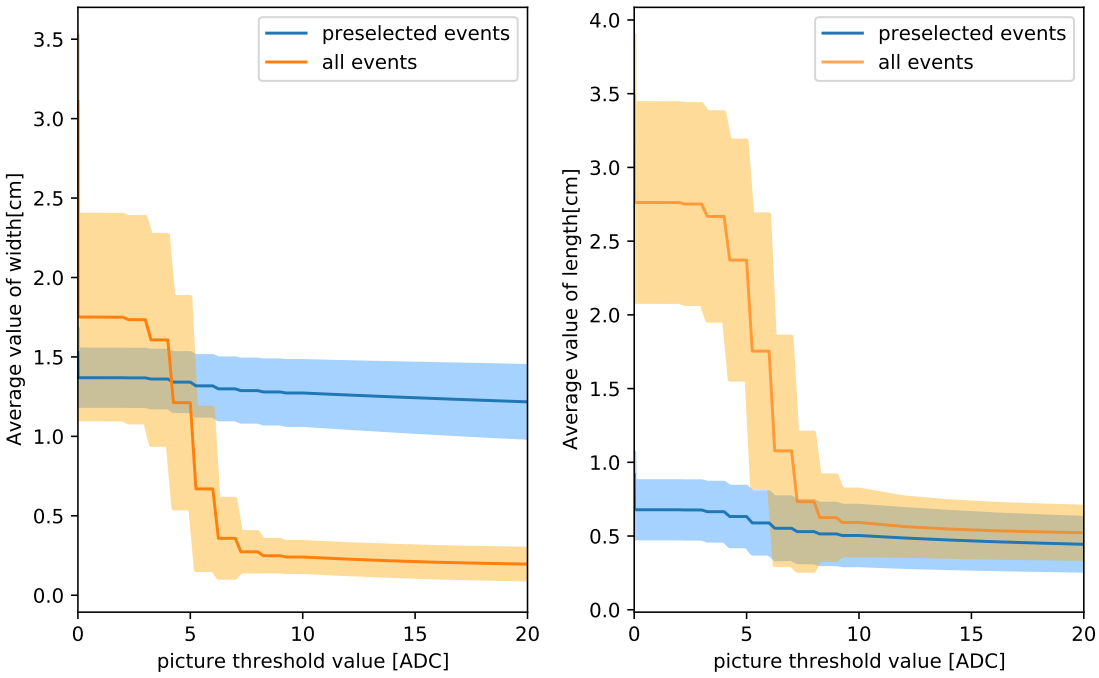

Figure 28: The average width and length and the standard derivation of the images as a function of the picture threshold.

6.2.3 Hillas analysis

After image cleaning with the determined limits, the next step is to perform a Hillas analysis on all images and compare their width and length before cleaning and after cleaning, which is illustrated in Fig. 29.

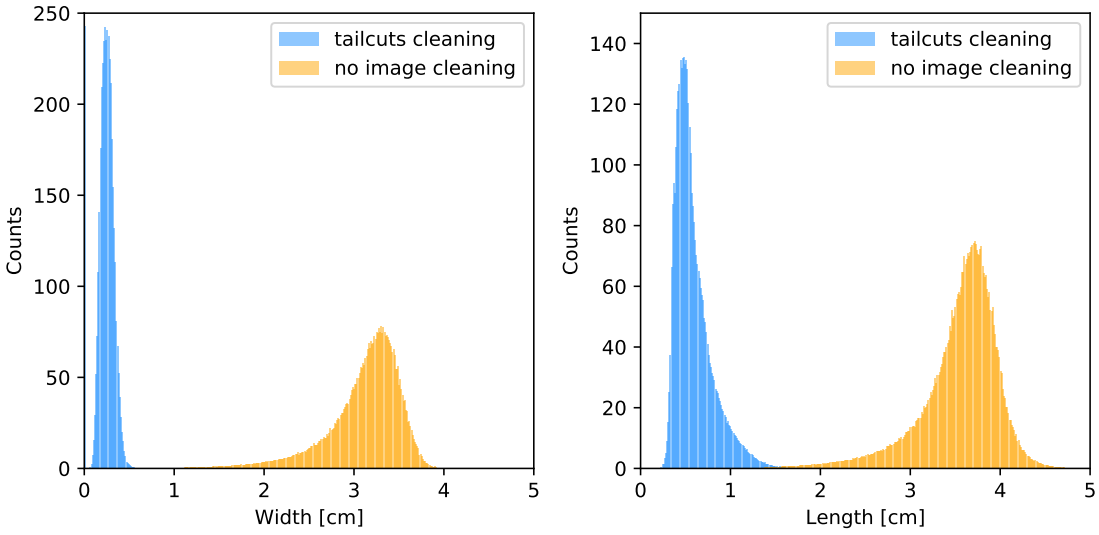

Figure 29: Hillas analysis without and with tail cuts cleaning

From 591098 simulated gamma shower events, only $\approx 96\,\%$ survived the image cleaning and the extraction of the hillas parameters. As expected, both the hillas width and length decrease after the cleaning since less outlying pixels are included. An example image (before and after cleaning) can be seen in fig. 30.

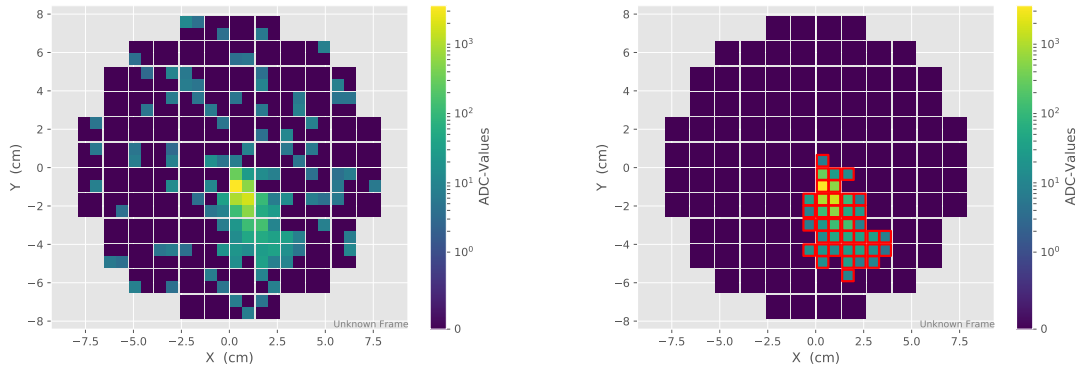

Figure 30: Intensity distribution of a gamma event in TinyTel camera before (left) and after image cleaning (right). The incoming gamma ray has a simulated energy of 51.74 TeV and an impact distance of 111.24 m

6.3 Event reconstruction

To investiage the event reconstruction capeability of TinyTel an array of 16 telescopes is simulated. The shower simulation parameters of gamma and hadron stayed the same as in the previous chapters. Figure 31 shows the layout of the array implemented in sim_telerray

which has a telescope spacing of 250 m between neighboring telescopes. This results in a 4 x 4 telescope array. This section is about reconstructing the impact point as well as the direction and energy of the primary particle. But before the event reconstruction is performed, some precuts are defined to improve the overall reconstruction performance.

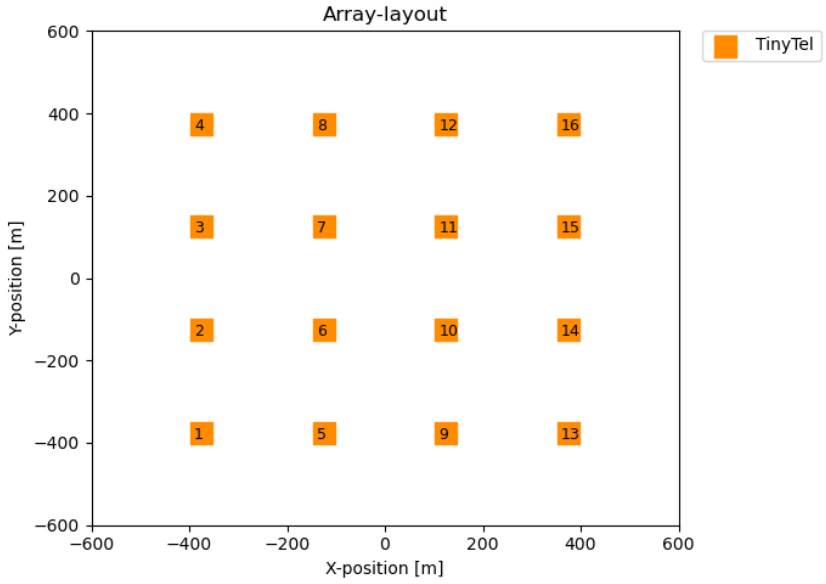

Figure 31: Array layout of 16 tiny sized telescopes TinyTel.

6.3.1 Stereo reconstruction

To reconstruct the geometry of the showers, several telescopes and their angle-preserving imaging are used. The principle of the reconstruction is shown in Figure 32. The images of all triggered telescopes are combined in a common coordinate system. This coordinate system can be in the camera plane or on the ground plane of the telescope array. The two-dimensional camera system, whose origin is in the focal plane of the cameras, is used to describe the image of the camera. Since the image of the camera represents the shower, the principal axis represents the direction of propagation of the particle shower, which is also the direction of its origin. That is, the intersection of the major axes of all telescopes indicates the direction when this occurs in the camera system, or the point of impact on the ground in the ground system.

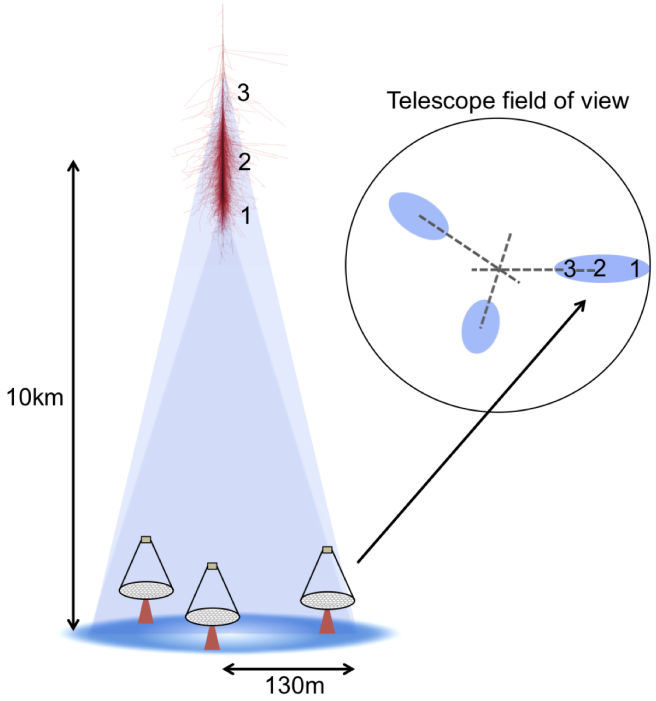

Figure 32: Illustration of the stereoscopic method. The primary particle triggers an atmospheric shower, which in turn generates Cherenkov radiation (figure taken from [26]).

When using multiple telescopes for the reconstruction, the telescopes that contain better information about the shower are weighted higher [27]. The angular resolution and the bias are used to validate the reconstruction.

Defining the preselection cuts

In the data processing chain of the telescope, the next step after cleaning the images and extracting the hillas parameters are the preselection cuts. The preselection cuts in this thesis are used on these three parameters, which are:

- The image size, also known as the image amplitude, is the number of measured photon electrons after image cleaning. In this thesis, two image size cuts, 60 pe ($\approx$ 360 ADC) and 120 pe ($\approx$ 720 ADC), were decided
- The distance of Center of gravity to the camera center is in this work referred to as Center of gravity cut. This parameter is used to remove events that are on the edge of the camera.
- Number of the triggered telescopes which are used in the reconstruction

Improvement of angular resolution and impact distance bias after precuts

A measure for accuracy of the impact point reconstruction is the bias and resolution of the reconstructed values.
The angular resolution is defined as the 68 % containment radius of angular separation between the simulated direction and the reconstructed one.
The relative bias on the other hand is defined as

$$\text{bias} = \frac{d_{reco} - d_{true}}{d_{true}} \tag{13}$$

where d_{reco} is the distance from the center of the telescope array to the reconstructed impact point and d_{true} is the distance from the center of the telescope array to the true impact point from the simulations. The spread of the relative bias is the resolution.

Center of gravity

First thing to do to improve the resolution is to find a suitable center-of-gravity-cut. The position of the center-of-gravity depends on the impact distance. Hence, with increasing distance between the telescope and the impact point the center of gravity of the shower ellipse moves towards the edge of the camera. The more the shower is away from the telescope, the less we get information of the telescope. Therefore, we are looking at the angular resolution as a function of the distance between camera center and center of gravity, which is shown in figure 33 for the image size cut 120 pe.

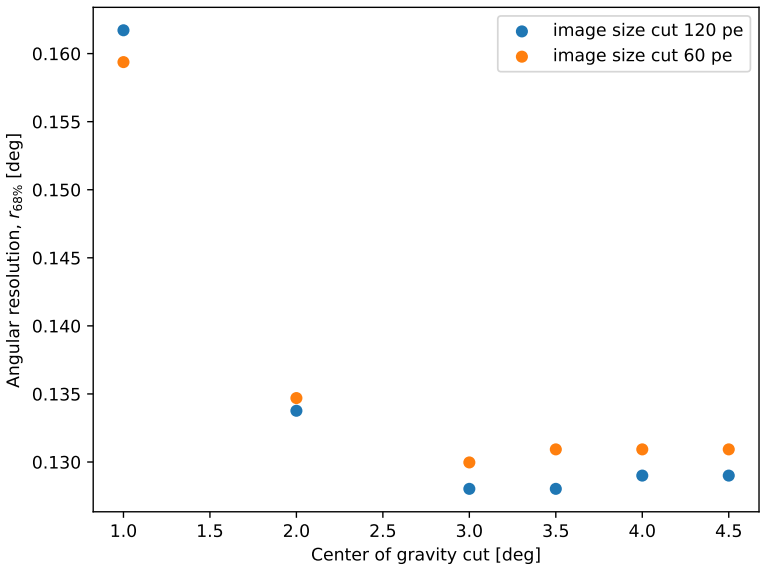

Figure 33: The angular resolution as a function of the Center-of-gravity cut for different image size cuts. Both data sets have the same cleaning level (= 40 ADC)

From the figure, we can set this cut at 4 deg for a field of view of 10 deg. For comparison, the maximal distance between camera center to the center-of-gravity in H.E.S.S (FoV 5 deg) is at 2 deg [25].

Cleaning level As discussed in section 6.2, for the geometrical reconstruction of the impact point on the ground a good image cleaning is needed. In this analysis, the picture threshold is set best at 10 ADC and the boundary threshold at 50 % of the picture threshold, since after these limits there is no significant change in the hillas parameters. But still it is necessary to investigate if the resolution can be improved by picture threshold. The picture threshold tested in this thesis are 10 ADC, 20 ADC and 40 ADC for both image size cuts. Figure 34 and figure 35 show the angular resolution and the relative bias as a function of the true energy with different picture thresholds which will be in the following referred to cleaning level for size cut 120 pe.

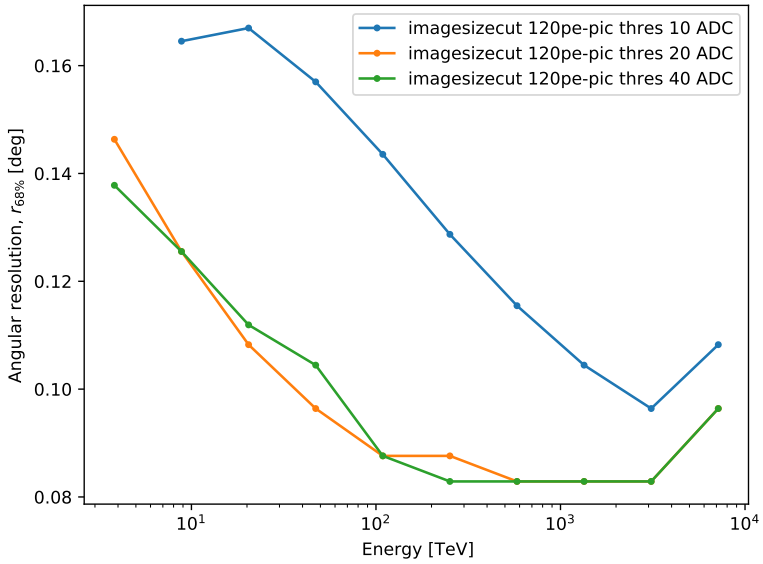

Figure 34: Angular resolution as a function of Monte-Carlo energy for an image size cut of 120 pe with different picture thresholds as cleaning level

For a higher cleaning level the reconstruction of the arrival direction of the primary particle in the case of the image size cut of 120 *pe* improves. In the cleaning level of 10 ADC are still some NSB pixels near the elliptical shape influencing the hillas parametrization that worsens the resolution of the reconstructed values. The same can be also seen in the spread of the bias. With a higher cleaning level the bias is closer to zero and the spread decreases. Similar results can also be seen for the case of the 60 pe size cut (Figure 36 and 37)

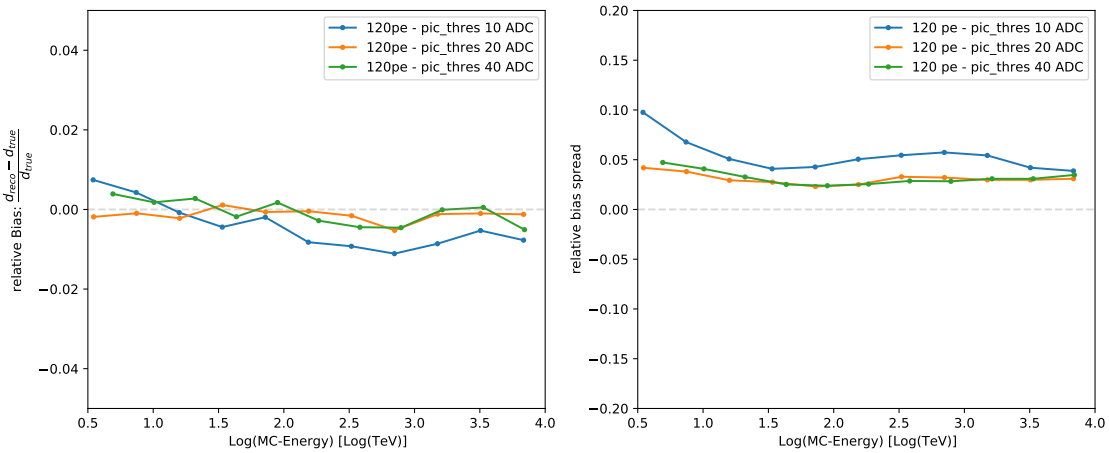

Figure 35: Relative bias and its spread as a function of Monte-Carlo energy for an image size cut of 120 pe with different picture thresholds as cleaning level

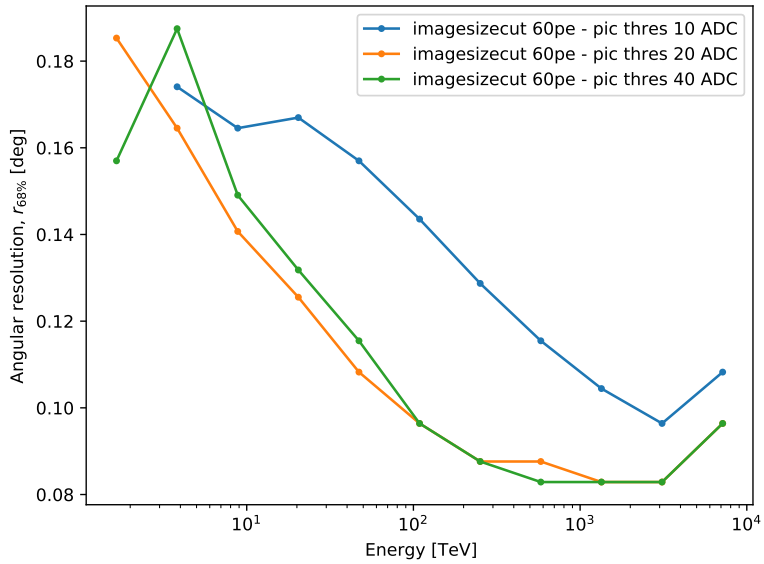

Figure 36: Angular resolution as a function of Monte-Carlo energy for an image size cut of 60 pe with different picture thresholds as cleaning level

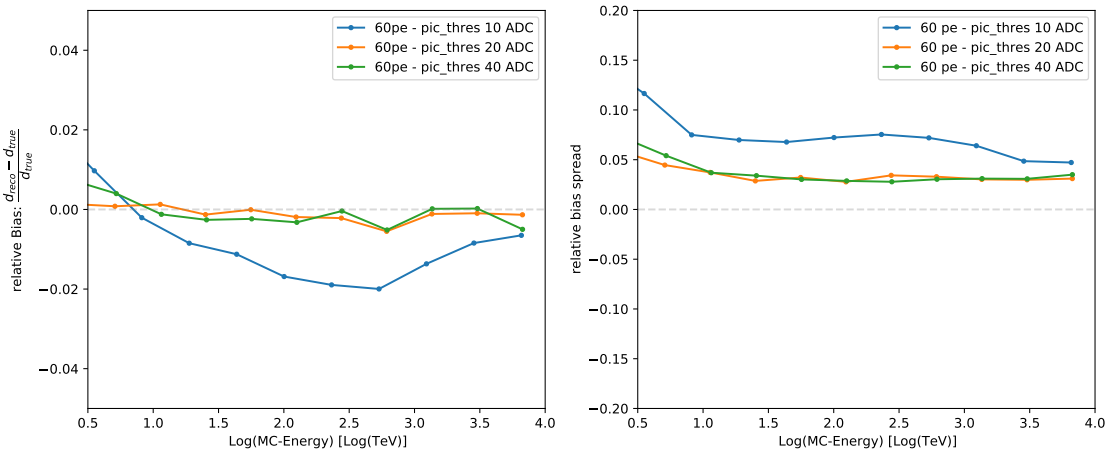

Figure 37: Relative bias and its spread as a function of Monte-Carlo energy for an image size cut of 60 pe with different picture thresholds as cleaning level

From the results it can be concluded that that the cleaning level influences the performance in the geometrical reconstruction and that the cleaning depends on the image amplitude cut. The higher the energy of the primary particle is, the larger and brighter the image is, therefore a smaller cleaning level can be chosen. In the following, for the image size cut of 120 pe a cleaning level of 20 ADC and for 60 pe a cleaning level of 40 ADC are chosen.

Number of used telescopes for hillas reconstruction If we compare the reconstructed impact distance with the true impact distance, which is shown in figure 38 (left) for the image size cut 120 pe with a cleaning level of 20 ADC, still large fluctuations in reconstructing the distance are occuring. If we increase the minimum number of used telescope for the reconstruction from two to three, most of the fluctuations are removed. That's because if the information of more telescopes is taken, the reconstruction is more precise. Furthermore, the angular resolution gets better with a higher minimum, as it is seen in 39. Therefore, the direction of the primary particle is reconstructed more accurately.

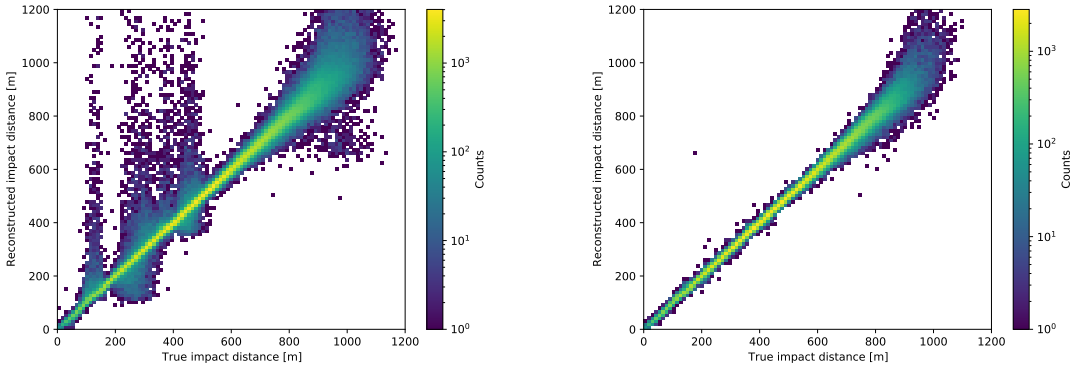

Figure 38: Comparison between true impact distance and reconstructed impact distance with more than two used telescopes (left) and more than three used telescopes (right)

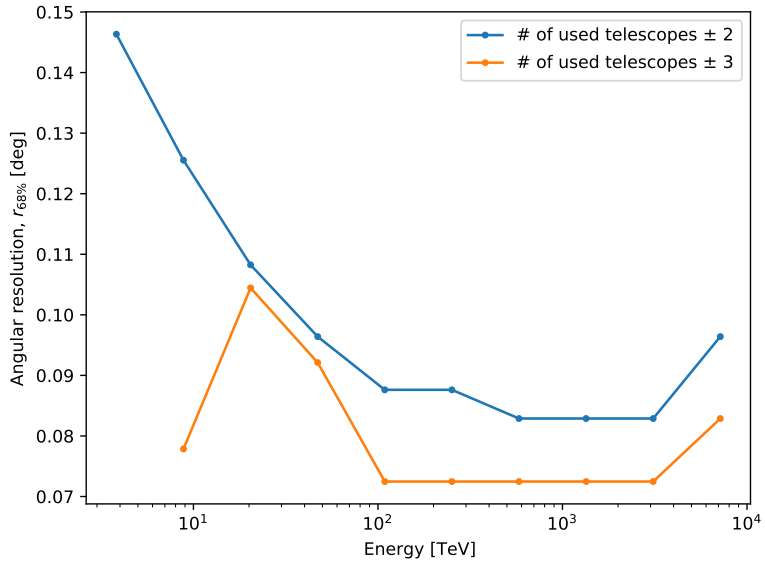

Figure 39: Angular resolution as a function of Monte-Carlo energy for an image size cut of 120 pe with picture threshold of 20 ADC but with different cuts on the number of used telescopes

6.3.2 Energy reconstruction

After the Hillas reconstruction, the next step is to determine the energy of the primary particle. For this, the reconstructed distance and the amplitude of the shower image are used. With the help of this information, lookup tables containing the simulated shower energy as a function of reconstructed distance and amplitude are generated. The lookup

table for gamma showers in the TinyTel telescope can be seen in Figure 40. In general, these lookups need to be done for various pointing directions because the zenith angle influences the shape and the shower development. In this work only one zenith angle (30 deg) is simulated. Therefore, the lookups are created for this zenith angle only. Additionally, these lookup tables are interpolated and smoothed out with a gaussian filter to reduce statistical fluctuations. But to get an approximate idea of the performance in energy reconstruction, the absolute values are decided.

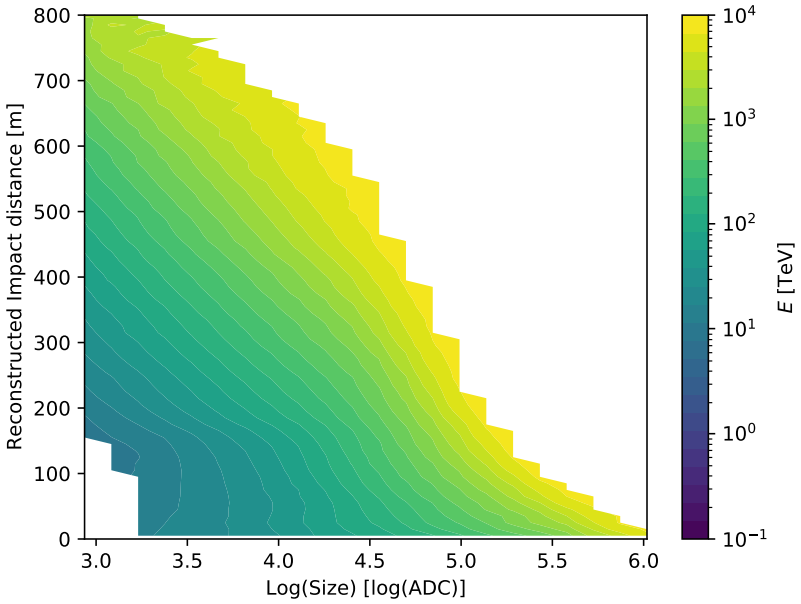

Figure 40: Unsmoothed energy lookup table for the gamma simulations with size cut 120 pe

The energy is determined for each individual telescope that participated in the event reconstruction. By weighting each telescope with its error in energy reconstruction, the average energy is calculated:

$$E_{\text{reco}} = \frac{\sum E_i \cdot \omega_i}{\sum \omega_i} \text{ with } \omega_i = \frac{1}{\sigma_i^2} \tag{14}$$

where E_i is reconstructed energy and σ_i is the corresponding energy error of telescope i [9]. To assess how precise the energy reconstruction of the telescope array is, energy resolution and the energy bias are considered.

Energy bias and energy resolution

The relative bias in reconstructed energy is plotted in figure 41 for the size cut of 120 pe (left) and the size cut of 60 pe (right), which show a well centered distribution, but with a slight asymmetric extension more directed to positive values. This slight shift is in full agreement with a gaussian fit. For the larger image size cut the mean of the relative bias is at 0.03 and has a resolution of 0.11 and for the lower image size cut the mean of the relative bias is at 0.04 and has a resolution of 0.13.

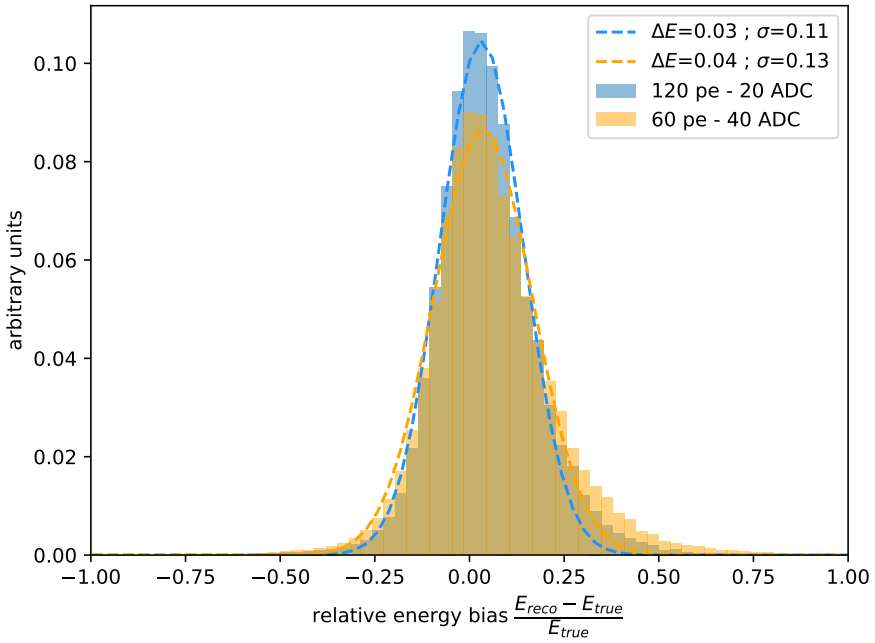

Figure 41: The relative energy bias for both size cuts with their corresponding energy resolution

Since the energy bias is dependent on the energy, another way to analyze it is to look at it as a function of the true energy (seen in figure 42).

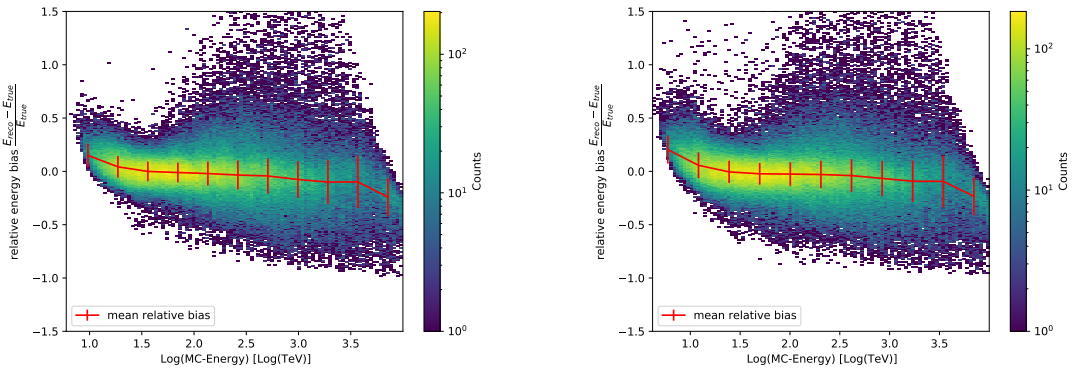

Figure 42: Two dimensional histogram of the relative energy bias and the monte-carlo energy with additional relative mean bias and spread (red) for sizecut 120 pe (left) and 60 pe (right)

At small energies, the graph shows a positive bias because the reconstructed energies are overestimated due to a selection effect. This means that only low energy showers that fluctuate upward survive the analysis and are entered into the lookup tables, while the others are discarded by, for example the size cut. This effect is also observed at high energies. Instead of the showers fluctuating upward, they fluctuate downward and cause a larger negative bias.

6.4 Gamma-Hadron-Separation

In reality, not only gamma-induced showers are recorded, but a large majority of the recorded events originate from hadronic cosmic rays. In order to reduce this much more numerous cosmic ray background while preserving a large fraction of gamma ray induced images, cuts on the image parameters have to be applied.
To distinguish the signal produced by gamma ray particles from background, the mean scaled width method is used. Since hadronic air showers show a stronger lateral spread and also more secondary sub-showers, the image parameters such as width and length are wider compared to electromagnetic air showers. Lookup tables for width and length are created using the gamma simulations, similar to the energy reconstruction technique. From the measured image parameters and the expected ones from the simulations, the reduced scaled width and length of a single shower event are calculated as follows [9]:

$$RSW_i = \frac{W_i - \langle W_i \rangle}{\sigma_{i,w}}\,, \quad RSL_i = \frac{L_i - \langle L_i \rangle}{\sigma_{i,l}} \tag{15}$$

with W_i and L_i being the width and length of telescope image i and $\sigma_{i,w}$ ($\sigma_{i,l}$) being the spread of the mean simulated width $\langle W_i \rangle$ (length $\langle L_i \rangle$). With results of each telescope

the weighted means (mean scaled width and length) are calculated [9]:

$$MSCW = \frac{\sum_i \omega_i \cdot RSW_i}{\sum_i \omega_i} \text{,with } \omega_i = \frac{\langle W_i \rangle^2}{\sigma_{i,w}^2}$$
$$MSCL = \frac{\sum_i \omega_i \cdot RSL_i}{\sum_i \omega_i} \text{,with } \omega_i = \frac{\langle L_i \rangle^2}{\sigma_{i,l}^2}$$

Moreover, a directional cut on θ^2, which was introduced as the squared angular separation between Monte-Carlo direction and reconstructed direction, can suppress additionally the background. As proposed from Stefan Klepser, the best cut on directional is 1.046 "times the 68 % containment radius" [28]. The assumed spectrum of gamma is 10 % of the Crab flux[25] and proton distribution follows along the cosmic ray flux (taken from [29]). A gamma ray signal consists of a number of excess events N_γ above the background level, which consist of air showers induced by cosmic-rays. Therefore, a statistical approach is used. This compares the difference between the number of events N_{on} in a circular region, whose size is defined by θ_{cut}, and the number of background events αN_{off}, which is estimated for this circular region based on the number of events N_{off} in an adequate off-source region. The excess can be determined by

$$N_\gamma = N_{\text{on}} - \alpha N_{\text{off}} \tag{16}$$

with the background normalisation factor α since exposure time or region sizes of On-region and off-region can differ from each other.
The significance of a signal can be determined by the Li & Ma method [30] as:

$$S_\gamma = \sqrt{2}\left(N_{\text{on}} \ln \frac{(1-\alpha)N_{\text{on}}}{\alpha(N_{\text{on}} + N_{\text{off}})} + N_{\text{off}} \ln \frac{(1+\alpha)N_{\text{off}}}{\alpha(N_{\text{on}} + N_{\text{off}})} \right) \tag{17}$$

For finding the perfect MSCW range for gamma showers, a one dimensional optimization is being performed on MSCW. Meaning, the optimized cut on MSCW achieves the highest significane. The MSCW distributions for both image size cuts is presented in 43.

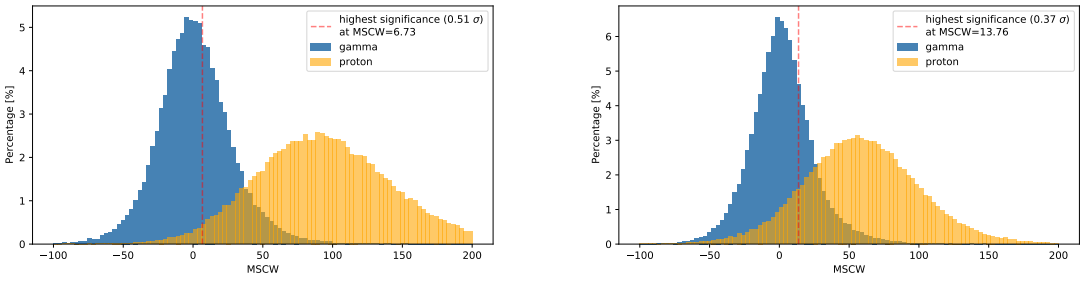

Figure 43: MSCW distribution of simulated gamma showers and proton showers for size cut 120 pe (left) and 60 (right)

6.5 Basic performance properties of TinyTel

Some the basic performance properties of the TinyTel telescopes are the instrument response functions and the sensitivity of the array. The IRF consists of the angular resolution, the energy resolution and the effective area. In the following sections, these three parameters will be compared before and after optimised cuts. Table 3 summarizes all used cut parameters from the previous sections.

	MSCW	θ^2	image size	cleaning	center of gravity cut
low	13.76	$0.0178\,\mathrm{deg}^2$	60 pe	40 ADC	4 deg
high	6.73	$0.0088\,\mathrm{deg}^2$	120 pe	20 ADC	4 deg

Table 3: Preselection and optimized cuts from previous sections

6.5.1 Instrument Responce Functions (IRF)

- After applying the preselection cuts and the optimized cuts the **angular resolution** shows an improvement, as it is plotted in figure 44.

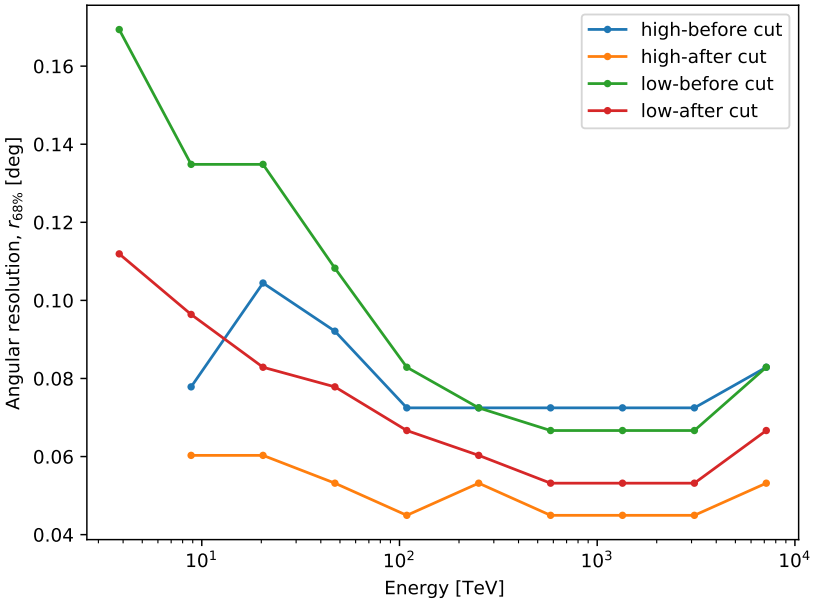

Figure 44: Angular resolution as a function of true energy before and after high and low

- The improvement of the **energy resolution** is presented in figure 45.

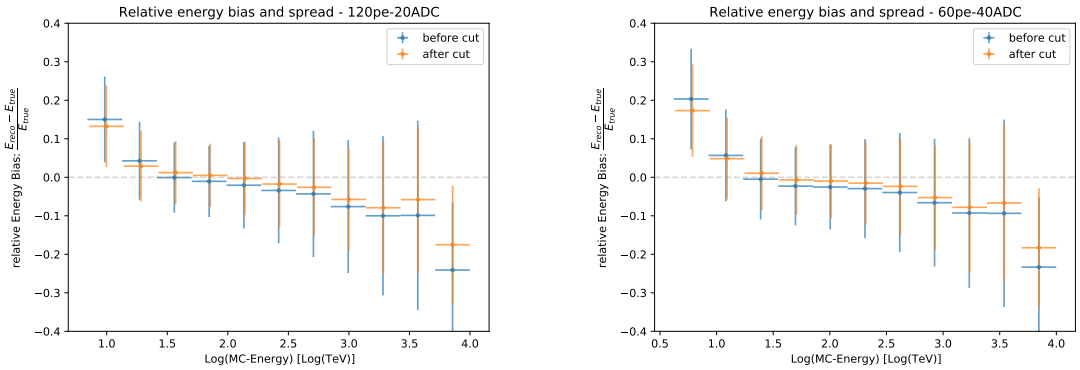

Figure 45: Relative energy bias and its spread as a function of true energy before and after cuts for 120 pe (left) and 60 pe (right)

- **The effective area** of a telescope array depends on the one hand on the trigger conditions and on the other hand on the applied cuts. It can be determined by the simulations and can be calculated as it follows:

$$A_{\text{eff}} = \frac{N_{\text{trigg}}}{N_{\text{all}}} \cdot A_{\text{sim}} \tag{18}$$

with the simulated area A_{sim}, the number of all simulated events N_{all} and the number of triggered events which survived selection cuts N_{trigg}. Moreover, the effective area depends on the simulated zenith angle, the shower energy of the primary particle and the azimuth angle because of the shower development. Figure 46 shows the effective area after applying different cuts on the simulated data for the size cut 120 pe (left) and for the size cut 60 pe (right).

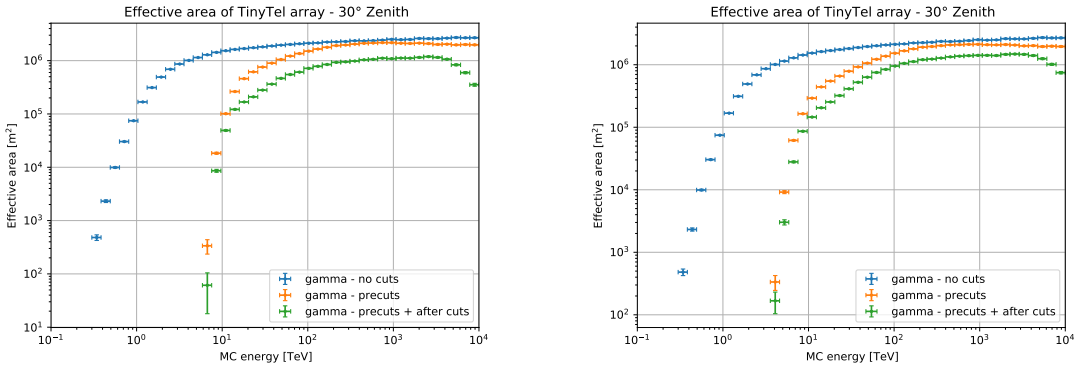

Figure 46: The effective area as a function of the true energy, where no cuts are performed as well as precuts and after precuts+optimized cuts for imagesize 120 pe (left) and 60 pe (right)

6.5.2 Sensitivity

The sensitivity of a detector indicates the minimum detectable flux of an object. Figure 47 shows the minimum detectable flux above energy E for a $5\,\sigma$ detection in 50 observation hours as a function of reconstructed energy for analysis using the reflected background method described. Each point represents an integrated sensitivity in the sense that it contains the minimum detectable flux above the energy indicated on the x-axis.[31]

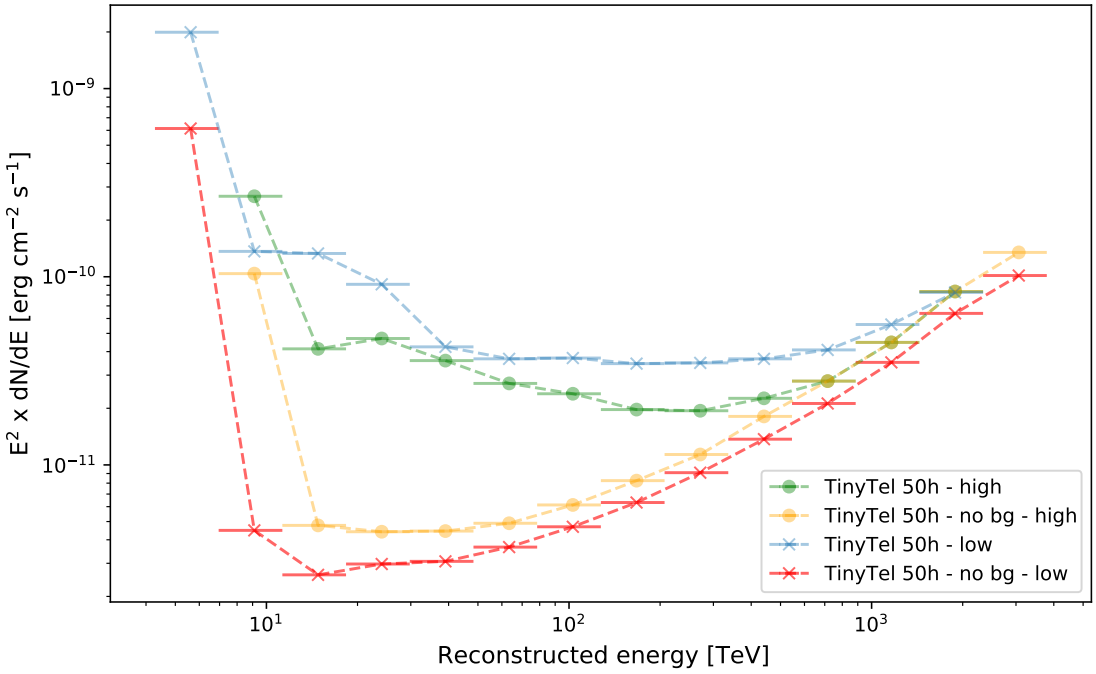

Figure 47: Sensitivity curves of TinyTel with high and low cuts. Additionally sensitivity curves with zero background are also presented here.(data taken from [32])

The sensitivity is shown for low cuts (blue) and high cuts (green). Assuming one can identify every gamma induced shower is known and the hadron induced shower can be neglected, the best case scenario can be investigated of the background rejection, where the background is assumed as zero. This is done for both cuts. To be mentioned, the minimal number of On-Counts is decided to be ten. From that, it can be followed that the background rejection of the telescope array is not efficient enough and needs improvement. Since in this thesis only the one dimensional optimization on the MSCW parameters is performed, a multidimensional approach is recommended, for example with a boosted decision tree training on all image parameters. In figure 48 the sensitivity of TinyTel is compared with operating project like H.E.S.S. and MAGIC and also the planned CTA. From this it can be seen that the TinyTel array with has similiar sensitivity as H.E.S.S. and MAGIC. Also the 16 telescopes array would be a good high energy extension of projects

like H.E.S.S., only if the background rejections is improved. If the number of telescopes is increased so that the sensitivity improves by a magnitude, then the project can also serve as an extension for CTA South at high energies.

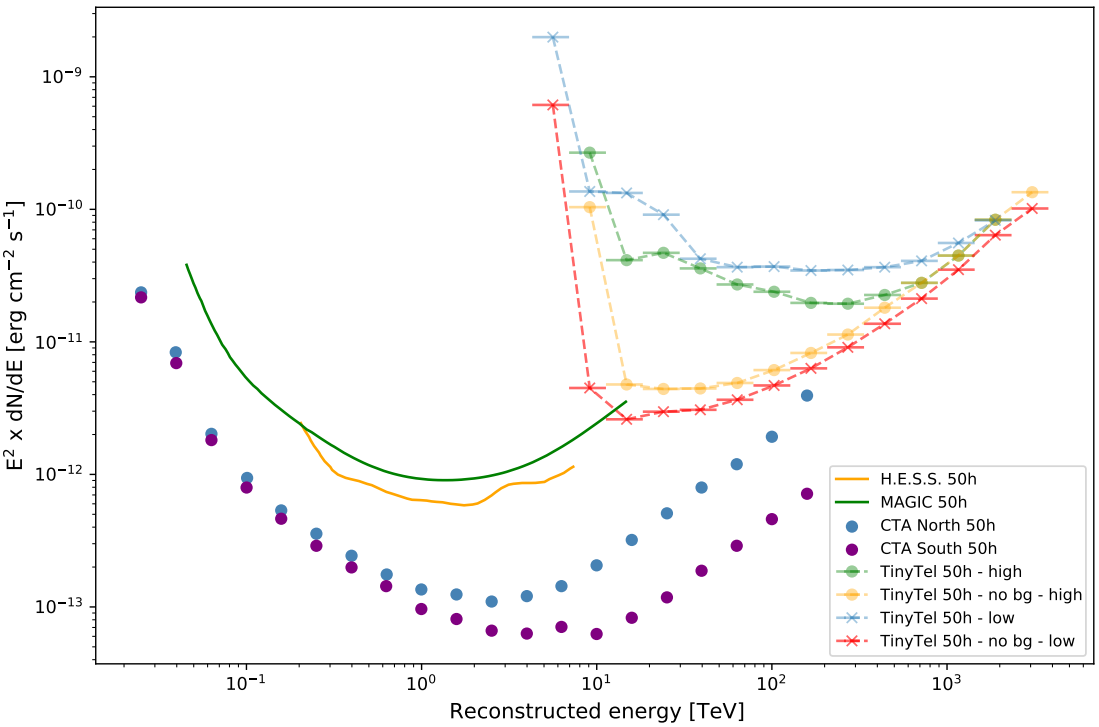

Figure 48: Comparison of TinyTel sensitivity curve with high and low cuts with sensitivity of MAGIC, H.E.S.S., CTA North and South

The signal efficiency and background rejection of the TinyTel array as a function of the reconstructed energy is shown in figure 49 for the high cuts and for the low cuts in figure 50. For both cases, one can see that the background rejection fraction decreases with increasing energy.

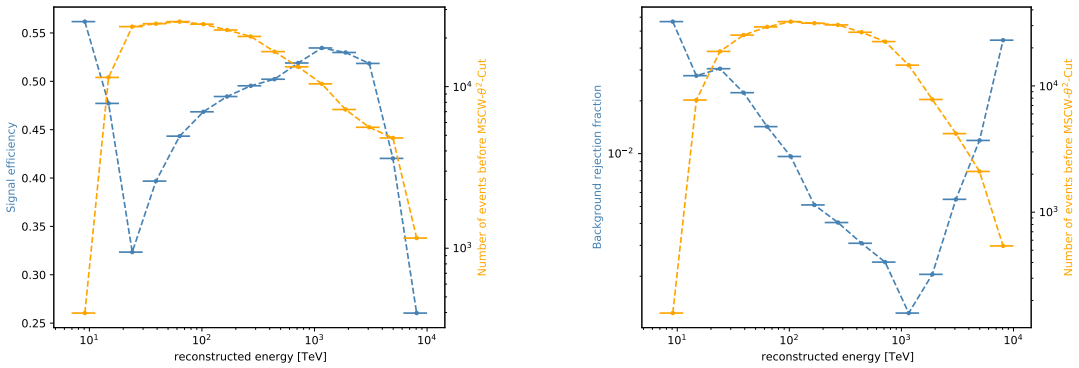

Figure 49: Signal efficiency and Background rejection fraction as a function of the reconstructed energy after performing the high cuts. Additionally, the number of background events and signal events before high cuts is plotted (orange)

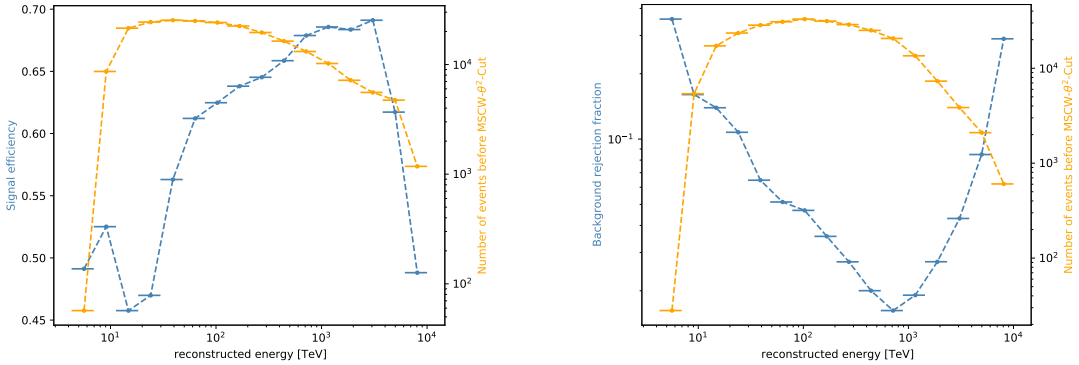

Figure 50: Signal efficiency and Background rejection fraction as a function of the reconstructed energy after performing the low cuts. Additionally, the number of background events and signal events before low cuts is plotted (orange)

7 Conclusion

The goal of this work was to achieve successful event reconstruction using a low-cost IACT telescope. In the first step, the existing IceAct telescope, a proposed candidate for the Gen2 upgrade and was used in the Namibia campaign for validation. However, it was shown in chapter 5.4 that a gamma-hadron separation according to the standard procedure is not possible due to the limitations of the setup. A solution to this problem would be to reduce the pixel size. It is worth mentioning that the telescope was not designed to perform an event reconstruction.

Subsequently, the idea of a new telescope was developed along the lines of the planned SST telescope of the CTA project, but in a scaled-down by a scaling factor of 0.42. This work created the tiny sized telescope called TinyTel and evaluated its the performance. After finished simulations, the minimum cleaning level was investigated (see section 6.2) and set at 10 ADC. After image cleaning, the event reconstruction of an array with 16 telescopes is analyzed. Thereby precut parameters like the center-of-gravity cut (4 deg), the image size cut (60 pe and 120 pe) and the minimum of the used telescopes (more than three) for the reconstruction of the entry direction of the primary particle and the impact point on the ground were defined. Due to a bias near zero and a small resolution, TinyTel shows a good stereo reconstruction in the energy range from ≈ 10 TeV to ≈ 1000 TeV. Energy look up tables were then created to reconstruct the energy of the primary particle. In the energy reconstruction of TinyTel the relative bias is below 4 % with a resolution of ≈ 11 % for the higher image cut and ≈ 13 % for the lower image cut. For gamma hadron separation, a straight cut on $MSCW$ and θ^2 being the squared angular separation between the reconstructed direction and the source direction is performed for low cuts (image size cut 60 pe, cleaning 40 ADC) as well as for higher cuts (image size cut 120 pe, cleaning 20 ADC). In the last chapter, the basic performance properties of TinyTel are analyzed after precuts and optimized cuts. An improvement in resolution of reconstructed parameters, like direction and energy of primary simulated particle, can be seen resulting in a successful event reconstruction. The sensitivity of TinyTel (see section 6.5.2) is analyzed in two cases: with and without background. As a result, the background rejection of the telescope is not sufficient which can be concluded from the sensitivity curve and the background rejection fraction per reconstructed energy. Since only a simple approach was taken in the gamma-hadron-separation, it is recommended to do a multi-variant cut optimization on the different image parameters and not only on $MSCW$ and θ^2 to improve the suppression of the background. Due to insufficient background suppression, it is not advisable to arrange TinyTel telescopes as the stand alone project. Using with a 16 telescope array, existing IACT projects such as H.E.S.S. can be extended to cover the high energy range of cosmic rays. With an even larger number of Telescopes TinyTel could also server as a high-energy extension for CTA. It must also be mentioned that the telescope can also be used very well for public outreach due to its size [33].

List of Figures

References

[1] C. Grupen. *Astroparticle Physics*. Vol. 2. Springer International Publishing AG, 2020. DOI: https://doi.org/10.1007/978-3-030-27339-2.

[2] Victor F. Hess. "Über Beobachtungen der durchdringenden Strahlung bei sieben Freiballonfahrten". In: *Phys. Z.* 13 (1912), pp. 1084–1091.

[3] Stefan Funk. "Ground- and Space-Based Gamma-Ray Astronomy". In: *Annual Review of Nuclear and Particle Science* 65.1 (2015), pp. 245–277. DOI: 10.1146/annurev-nucl-102014-022036. eprint: https://doi.org/10.1146/annurev-nucl-102014-022036.

[4] Tim Niggemann. "The silicon photomultiplier telescope FAMOUS for the detection of fluorescence light". Dissertation. Aachen: RWTH Aachen University, 2016, 1 Online–Ressource (viii, 215 Seiten) : Illustrationen, Diagramme. URL: https://publications.rwth-aachen.de/record/673852.

[5] Particle Data Group et al. "Review of Particle Physics". In: *Progress of Theoretical and Experimental Physics* 2020.8 (Aug. 2020). 083C01. ISSN: 2050-3911. DOI: 10.1093/ptep/ptaa104. eprint: https://academic.oup.com/ptep/article-pdf/2020/8/083C01/34673740/rpp2020-vol2-2015-2092_18.pdf.

[6] Johannes Blümer, Ralph Engel, and Jörg R. Hörandel. "Cosmic rays from the knee to the highest energies". In: *Progress in Particle and Nuclear Physics* 63.2 (Oct. 2009), pp. 293–338. ISSN: 0146-6410. DOI: 10.1016/j.ppnp.2009.05.002.

[7] S. Thoudam et al. "Cosmic-ray energy spectrum and composition up to the ankle: the case for a second Galactic component". In: *Astronomy & Astrophysics* 595 (Oct. 2016), A33. ISSN: 1432-0746. DOI: 10.1051/0004-6361/201628894.

[8] H. Bethe and W. Heitler. "On the Stopping of fast particles and on the creation of positive electrons". In: *Proc. Roy. Soc. Lond. A* 146 (1934), pp. 83–112. DOI: 10.1098/rspa.1934.0140.

[9] David Jankowsky. "Measurement of the Cosmic Ray Proton Spectrum with H.E.S.S. and Characterization of the TARGET ASICs for the CTA". PhD thesis. Erlangen - Nuremberg U., 2020.

[10] F. Aharonian et al. "High energy astrophysics with ground-based gamma ray detectors". In: *REPORTS ON PROGRESS IN PHYSICS Rep. Prog. Phys* 71 (Sept. 2008), pp. 96901–56. DOI: 10.1088/0034-4885/71/9/096901.

[11] N. W. Hermann Kolanoski. *Teilchendetektoren*. Vol. 1.ed. Springer Spektrum, 2016.

[12] Mathieu de Naurois and Daniel Mazin. "Ground-based detectors in very-high-energy gamma-ray astronomy". In: *Comptes Rendus Physique* 16.6-7 (Aug. 2015), pp. 610–627. ISSN: 1631-0705. DOI: 10.1016/j.crhy.2015.08.011.

[13] J.A. Hinton and W. Hofmann. "Teraelectronvolt Astronomy". In: *Annual Review of Astronomy and Astrophysics* 47.1 (2009), pp. 523–565. DOI: 10.1146/annurev-astro-082708-101816. eprint: https://doi.org/10.1146/annurev-astro-082708-101816.

[14] Heinrich J. Völk and Konrad Bernlöhr. "Imaging very high energy gamma-ray telescopes". In: *Experimental Astronomy* 25.1-3 (Mar. 2009), pp. 173–191. ISSN: 1572-9508. DOI: 10.1007/s10686-009-9151-z.

[15] The CTA Consortium. *Cherenkov Telescope Array: The Next Generation Gamma-ray Observatory*. 2017. arXiv: 1709.05434 [astro-ph.HE].

[16] CTA observatory. URL: https://www.cta-observatory.org/ (visited on 08/20/2021).

[17] CTA observatory. *Small-Sized Telescope*. 2019. URL: https://www.cta-observatory.org/project/technology/sst/ (visited on 08/20/2021).

[18] Konrad Bernlöhr. "Simulation of imaging atmospheric Cherenkov telescopes with CORSIKA and sim_telarray". In: *Astroparticle Physics* 30.3 (2008), pp. 149–158. ISSN: 0927-6505. DOI: https://doi.org/10.1016/j.astropartphys.2008.07.009.

[19] *cta-observatory/pyirf: v0.4.0*. Version v0.4.0. DOI: 10.5281/zenodo.4304466.

[20] J. Schäfer. *private communication (the description of DACT will be part of J. Schäfer's PhD thesis at FAU Erlangen-Nürnberg)*. 2020.

[21] Stefan Dietz. "Set-up, South Pole field test and energy threshold determination of the Erlangen design of an IceAct telescope." Erlangen - Nuremberg U., 2019.

[22] A. Zink. *private communication (FAU Erlangen-Nürnberg)*. 2020.

[23] Karl Kosack et al. *cta-observatory/ctapipe: v0.8.0*. Version v0.8.0. May 2020. DOI: 10.5281/zenodo.3837306.

[24] A. M. Hillas. "Cerenkov Light Images of EAS Produced by Primary Gamma Rays and by Nuclei". In: *19th International Cosmic Ray Conference (ICRC19), Volume 3*. Vol. 3. International Cosmic Ray Conference. Aug. 1985, p. 445.

[25] F. Aharonian et al. "Observations of the Crab nebula with HESS". In: *Astronomy & Astrophysics* 457.3 (Sept. 2006), pp. 899–915. ISSN: 1432-0746. DOI: 10.1051/0004-6361:20065351.

[26] Jamie Holder. *Atmospheric Cherenkov Gamma-ray Telescopes*. 2015. arXiv: 1510.05675 [astro-ph.IM].

[27] W Hofmann. "Comparison of techniques to reconstruct VHE gamma-ray showers from multiple stereoscopic Cherenkov images". In: *Astroparticle Physics* 12.3 (Nov. 1999), pp. 135–143. ISSN: 0927-6505. DOI: 10.1016/s0927-6505(99)00084-5.

[28] S. Klepser. "The optimal on-source region size for detections with counting-type telescopes". In: *Astroparticle Physics* 89 (Mar. 2017), pp. 10–13. ISSN: 0927-6505. DOI: 10.1016/j.astropartphys.2017.01.005.

[29] Sanuki Tomoyuki. “A Precise Measurement of Cosmic-Ray Proton Spectrum with BESS Spectrometer”. In: *26th International Cosmic Ray Conference (ICRC26), Volume 3*. Vol. 3. International Cosmic Ray Conference. Aug. 1999, p. 93.

[30] T. -P. Li and Y. -Q. Ma. “Analysis methods for results in gamma-ray astronomy.” In: 272 (Sept. 1983), pp. 317–324. DOI: 10.1086/161295.

[31] T. Hassan et al. “Monte Carlo performance studies for the site selection of the Cherenkov Telescope Array”. In: *Astroparticle Physics* 93 (July 2017), pp. 76–85. ISSN: 0927-6505. DOI: 10.1016/j.astropartphys.2017.05.001.

[32] Daniel Mazin. *The Cherenkov Telescope Array*. 2019. arXiv: 1907.08530 [astro-ph.IM].

[33] J. Hinton S. Funk. *private communication (FAU Erlangen-Nürnberg and MPIK Heidelberg)*. 2020.

Acknowledgements

Finally, I would like to thank everyone who supported me during this thesis and during this pandemic. In particular, I would like to thank:

- Prof. Dr. Stefan Funk for giving me the opportunity to work on this very exciting topic, the supervision of this thesis and his helpful comments in our biweekly meetings and in our ECAP-Chat discussions.
- Jim Hinton and Richard White from MPIK Heidelberg for the big interest in my results on the simulations of TinyTel and the very helpful comments in our meetings.
- Johannes Schäfer for your support during this thesis and for your help (even at the latest hours or on the weekends)
- Benjamin Schwab as my office fellow. Together with Johannes I had a great time in our office and also in our virtual coffee breaks during home office.
- my fellow students, Anna-Luisa, Moritz and Michael, whom i have known since the first semester and became great friends, which supported me during my studies and helped me to manage my studies and my competitive dancing.
- my parents and my brother Josip for their support during this thesis and throughout all my studies.

Erklärung

Hiermit bestätige ich, dass ich diese Arbeit selbstständig und nur unter Verwendung der angegebenen Hilfsmittel angefertigt habe.

Erlangen, den 13. 09. 2021